\$50 CONTRACTOR OF THE SECOND S

Contents lists available at ScienceDirect

Ocean Engineering

journal homepage: www.elsevier.com/locate/oceaneng





Modeling the motion of large vessels due to tsunami-induced currents

Aykut Ayca a,b,*, Patrick J. Lynett a

- a Department of Civil and Environmental Engineering, Tsunami Research Center, University of Southern California, Los Angeles, CA, USA
- ^b Now at FM Global, 1151, Boston-Providence Turnpike, Norwood, MA, USA

ARTICLE INFO

Keywords:
Tsunami currents
CFD
Shallow water equations
Transport
Coupling
Ports

ABSTRACT

This paper describes a model developed to predict the general behavior of large vessels under energetic tsunami conditions using established regional-scale tsunami models. The methodology is based on a two-way coupled approach to account for the interaction between vessels and flow, which becomes increasingly important in restricted waters. A shallow water hydrodynamic solver is modified to include vessels as horizontal pressure distributions, and friction coefficients are adjusted accordingly at the locations of vessels to account for the effects of skin friction. Adequacy of these modifications are then tested against a benchmark case designed in OpenFOAM®, and comparisons demonstrate the modified shallow water solver's ability to provide a reasonable realization for energetic flow passing a floating object. A vessel transport model coupled with the hydrodynamic solver is based on the linear equations of ship motion with three degrees of freedom (surge, sway and the yaw). Finally, the model is equipped with a collision solver founded on the concept of the conservation of momentum and impulse. Results from two large scale applications of the developed tool are presented. These analyses revealed that the flow in and around the ports is indeed strongly affected by the presence of vessels. Also, it is observed that the model can approximate the ship's behavior, but at the same time the model results are very sensitive to the initial choice of the input parameters due to the chaotic nature of the process.

1. Introduction

With the growth of the maritime industry, the sizes of the container ships and the amount of cargo transported with them have greatly increased over the last 60 years (Borrero et al., 2015a,b). As the latest tele-tsunamis have demonstrated, maritime communities are particularly vulnerable to the effects of tsunami-induced currents. We have seen that even when there is no or little inundation, the currents generated by tsunami surges can potentially cause significant damage to maritime facilities (Lynett et al., 2012, 2014, 2014). These observations have led to new questions regarding the adverse effects of tsunamis. These unwanted and often un-avoidable effects can range from small damage to vessels and infrastructure to the complete destruction of harbors (Wilson et al., 2012, 2013; Dengler et al., 2008).

Over the past few years, unfavorable nearshore effects of tsunami-induced currents from far-field sources have been reported from many locations around the world. Several incidents occurred during the 2004 Indian Ocean tsunami and were documented in detail by Okal et al. (2006a, 2006b; 2006c). The most astounding of these events took place in Port of Salalah, Oman, where an approximately 300-m long container

ship broke all its twelve mooring lines due to strong currents generated near the loading berth. The vessel drifted on the currents, spinning uncontrollably for hours both in and around the harbor until the vessel beached on a sandbar outside of the port. There was not any overland flooding or inundation in the Port of Salalah as the maximum tsunami amplitude during the event was about 1.5-m. However, the currents generated locally by the relatively small tsunami were strong enough to pull the large container ship off the dock. The currents near the vessel were estimated to be around 4-5 m/s by numerical simulations of the event (Lynett et al., 2012). In the wake of the Indian Ocean tsunami, a similar instance was also reported in Leport, Réunion Island. A 196-m container ship, the MSC Uruguay, broke all its mooring lines and drifted inside the harbor, striking and damaging gantry cranes on a nearby dock (Okal et al., 2006b). Likewise, in the Port of Toamasina, Madagascar, a 50-m freighter wandered through the harbor for nearly 3 h after breaking its moorings (Okal et al., 2006c). All these incidents occurred well after the arrival of the tsunami that was described as not flooding the port facilities. This is important to consider, because practitioners without specific experience in tsunami hydrodynamics may stop computations shortly after the maximum runup of the first or

^{*} Corresponding author. Department of Civil and Environmental Engineering, Tsunami Research Center, University of Southern California, Los Angeles, CA, USA. *E-mail address:* ayca@usc.edu (A. Ayca).

second wave is reached. Eddies can persist for days, and this makes computations more unreliable, as numerical errors can accumulate.

The Tohoku tsunami that was triggered by the great Tohoku-oki earthquake ($M_{\rm w}=9.0$) was documented quite well through comprehensive observations and instrumental measurements. Although current speed measurements were not widespread along the Pacific Rim, there are a few data sets available. In the extreme near field, Fritz et al. (2012) analyzed the videos recorded by two eyewitnesses in Kesennuma, Japan to determine tsunami current speeds. Their analysis revealed that the current speeds in Kesennuma Bay reached up to 11 m/s, making navigation impossible. However, in the far field, harbors and bays in the Hawaii Islands (Cheung et al., 2013), several harbors in New Zealand (Borrero et al., 2013; Lynett et al., 2012), and some harbors in the Galapagos Islands, including the largest port of the country, Puerto Ayora (Lynett et al., 2013), also experienced strong currents and damage related to these currents, even though the incoming tsunami heights were relatively small.

The assessment of seakeeping and maneuverability of large vessels has always been of high interest to researchers whether they are in unrestricted (water depth \gg draft of the ship) waters, or in ports and canals where they are restricted in both depth and breadth. However, recent incidents in ports as described above show that the maneuvering capabilities of vessels can become very limited when they are captured by strong currents, and within eddies in particular. The vessels that break free and drift off in and around the port during tsunamis generally exhibit apparently random behavior, and thus poses a great risk of impact hazard to the port.

Therefore, we concern ourselves in this work with reports of large vessels that go out of control in and around ports under hazardous conditions caused by tsunamis. To develop mitigation plans for these situations, we can rely on numerical modeling. Yet, the first-order approaches, where the flow and object transport are decoupled, would not be sufficient in these cases. The reason being is that in shallow and/or restricted waters (e.g. narrow waterways, ports, harbors, bays) the ratio of vessel draft to water depth approaches 1. This, in essence, leads to reduced effective flow depth and accelerated current speeds near vessels, which consequently increases the current force acting on the hull. Nonetheless, this interaction should be accounted for while developing models for this matter, although it was ignored in most of the earlier published efforts (e.g. Tomita and Honda, 2011; Sakakibara et al., 2010; Kobayashi et al., 2011) that study large vessel motion during tsunamis.

To address this issue, here we present a large-vessel transport model that is two-way coupled with a hydrodynamic numerical model allowing the interaction between the flow and vessel. The hydrodynamic parameters come from a shallow water solver, the application of the "method of splitting tsunami" (MOST) numerical model (Titov and Synolakis, 1998). Although the sophistication of MOST initially may not seem sufficient for this problem, its computational efficiency in geophysical scale $(\mathcal{O}(km))$ over higher order Boussinesq-type (e.g. Kim et al., 2009; Shi et al., 2012) or non-hydrostatic solvers (e.g. Ma et al., 2012) and as well as its' proven accuracy in modeling tsunami-induced currents (Lynett et al., 2014; Kalligeris et al., 2015) alludes it as the ideal tool. Aside from Eulerian based methods, models solving incompressible or weakly compressible versions of Navier-Stokes equations in a Lagrangian framework like smoothed particles hydrodynamics (SPH) are becoming popular in an attempt to deal with fluid-structure interaction. Various studies (e.g., Wu et al., 2016; Rakhska et al., 2019; Zhan et al., 2019; Sun et al., 2021 and references therein) employ SPH in 3D to model flows interacting with different objects of varying sizes. Although all these models demonstrate that they can capture the flow-structure interaction accurately with a great level of detail, they mainly concern with very small length scales ($\mathcal{O}(m)$). Additionally, the accuracy of SPH models depends heavily on the resolution, which increases the number of particles to be included in the calculations drastically, and eventually it gets impractical to utilize SPH for larger scale objectives due to high computational demand.

Unlike numerically expensive 3D models, when modeling the wood transport during flash floods Ruiz-Villanueva et al. (2014a, 2014b) also utilized a 2D hydraulic solver and included the feedback from the wood logs into hydrodynamic calculations by adding the drag force acting on woods as a source term to the momentum equations. More recently, Xiong et al. (2020) presented a coupled transport model in 1D, where they employed discrete element modeling (DEM) method to calculate forces on debris particles. They also achieved fluid-particle coupling by adding forces exerted on the debris back into momentum equation. In this study, instead of adding the reactive forces to momentum equations, we introduce vessels as pressure disturbances into the hydrodynamic calculations to attain flow-vessel interactions, which accounts for the form drag produced by their presence in the flow. Furthermore, we manipulate manning's coefficient locally to include the impact of skin friction, which becomes important when dealing with large vessels. Finally, a collision model integrated into the coupled model to resolve collisions between vessels or vessels and port structures (e,g, berths, quays etc.).

The motivation for this study comes from the observations discussed above and the hope to be able to provide quantitative guidance to authorities on potential vessel motions during tsunamis. We, however, remark here that the objective of this study is to capture the general behavior of large vessels under energetic tsunami conditions using established regional-scale tsunami models. We explain our approach to the problem, specifically the modifications made to MOST, and how these modifications enabled MOST to attain the interaction between the flow and large vessels as well as its' limitations along with the large vessel transport and collision models in Chapter 2. Small scale model validation exercises are discussed in Chapter 3 and, the application of the model in geophysical scale is given in Chapter 4.

2. Methods

2.1. Hydrodynamic numerical tool

The MOST model has been used extensively for tsunami hazard assessments in the United States and is currently used for operational tsunami forecasting at the NOAA Pacific Marine Environmental Laboratory (PMEL). Variants of the MOST model have been in constant use for tsunami hazard assessments in California since the mid-1990s (Titov et al., 2016). MOST solves the classical 2+1 nonlinear shallow water (NSW) equations using a finite difference scheme.

$$h_t + (uh)_x + (vh)_v = 0$$

$$u_t + uu_x + vu_y + gh_x = gd_x - Du$$

$$v_t + uv_x + vv_y + gh_y = gd_y - Dv$$

where $\eta(x,y,t)=$ water surface elevation, d is the water depth, $h(x,y,t)=\eta(x,y,t)+d(x,y,t)$, u(x,y,t) and v(x,y,t) are the depth-averaged velocities. D(h,u,v) is the drag coefficient computed by the quadratic equation

$$D(h, u, v) = \frac{f}{h} \sqrt{u^2 + v^2}$$

where f is the nondimensional friction coefficient, related to Manning's roughness coefficient, n, as $f = n^2 g / h^{1/3}$ (Satake, 1995). More thorough information about the theoretical background and the validation of MOST is provided in Titov and Synolakis (1998), and Burwell et al. (2007). Using the long wave assumption, MOST approximates 3D processes with two horizontal dimension (2HD) equations.

As a final note about the verification of the MOST (Lynett et al., 2014), conducted a sensitivity analysis to understand the accuracy of MOST in resolving complex nearshore hydrodynamics, where they have

compared the MOST results with a high-order fully nonlinear Boussinesq-type model (COULWAVE) and with available field data. They found out that MOST matches the tsunami amplitude phase patterns for the first several hours and the amplitude envelope for at least 24 h after the first arrival of the tsunami. Likewise, MOST can also match the current velocities extracted from eyewitness videos. On average, current velocities predicted by MOST are 10-20% higher than COUL-WAVE results, which leaves MOST on the conservative side. As a result of these observations, they concluded that MOST was sufficiently capable of modeling tsunami-induced currents using a 1/3 arcsec (~10 m) grid size. During the 2015 Chilean tsunami. Kalligeris et al. (2016) made in-situ measurements of current speeds in Ventura Harbor California. In their comparison of MOST output to measured data, they found that MOST matched the phase of the measurement well, and the velocity estimates by MOST remain in the envelope of the measurements.

2.2. Inclusion of ships as pressure distributions

There are several established techniques to model fluid-structure interaction. The Immersed Boundary (IB) method, probably the most popular, is discussed in Peskin (2002) and has been used extensively in studies dealing with fluid-structure interaction. An example application of IB method is presented in Ma et al. (2016), where they apply this method to include fluid-structure interaction in their nonhydrostatic σ – coordinate model. Earlier last decade, Kamrin et al. (2012) established a method called the Reference Map Technique (RMT), in which both the fluid and the solid are defined in the Eulerian reference frame. Recently, Bellotti and Theillard (2019) integrated RMT to an incompressible Navier-Stokes solver to model two-phase flows, which allows for the interaction of either two different fluids or one type of fluid with solid objects. However, both IB method and RMT approximate the fluid-structure interaction by enforcing a no-slip condition over the boundary of the solids. Yet, this aspect of IB and RMT methods becomes a limitation in 2HD (e.g. MOST) models when attempting to model the interaction between the fluid and the floating objects. An object with a no-slip boundary condition in a 2HD model will block the flow that is supposed to pass underneath the floating object; hence the essence of the problem will change; in general, 2HD models employ free slip conditions on solid boundaries due to their inherent inability to resolve detailed boundary layer processes. Due to this fact, the fluid-structure interaction in this study is attained through modeling vessels as free surface pressure disturbances.

It is a common approach to define vessels as horizontal pressure disturbances when studying waves generated by moving ships (e.g. Akylas, 1984; Ertekin et al., 1986; Liu and Wu, 2004; Bayraktar-Ersan and Beji, 2013; David et al., 2017). Following approaches found in the literature, we modify the momentum equations in the x and y directions in MOST by adding free surface pressure terms defined in the horizontal plane:

$$u_t + uu_x + vu_y + gh_x = gd_x - Du - \frac{1}{\rho} \frac{\partial P_0}{\partial x}$$

$$v_t + uv_x + vv_y + gh_y = gd_y - Dv - \frac{1}{\rho} \frac{\partial P_0}{\partial v}$$
 6

where $P_0(x,y)$ is the free surface pressure disturbance. With this pressure disturbance, the initial vessel profile condition becomes:

$$u = 0, \ v = 0, \ \eta = -\frac{P_0}{\rho g}$$

Of particular interest to this study, as stated earlier, is to develop a model that can reasonably resolve the flow around vessels. Interaction of the crossflow with the vessels results in acceleration in the flow passing underneath, or the wakes generated behind the vessel. The interactions

are primarily driven by the total drag acting on the vessel, which has 2 major components: *i*) friction drag due to viscous resistance of the water, *ii*) form drag due to shape of the ship hull (Sorensen, 1973). The effect of the form drag is accomplished by including the pressure gradient terms $(\partial p/\partial x, \partial p/\partial y)$ in the momentum equations. Here we further argue that the friction drag can also be approximated by increasing the shear stress locally at the grid points at which pressure gradients are non-zero. In the MOST model, this local increase in stress is captured through a local increase in the Manning's "n" parameter, which attempts to account for the vessel skin friction. Though, the amount of this local increase cannot be arbitrarily decided, therefore a benchmark test designed in Open-FOAM for calibration and model validation purposes, presented in Section 3.2.

2.3. Collision model

The three main modeling challenges in a collision model are 1) the detection of the collisions, 2) calculating the required post-collision velocities to break the contact, and 3) computing the necessary contact forces that will lead to proper changes in velocities. The details of the collision detection algorithm and the collision solver that tackle these problems in a physically correct manner will be explained in this section.

2.3.1. Collision detection

The literature in collision detection is quite rich due to significant contributions of computer graphics and robotics researchers. One of the generally accepted and applied methods is called the Separation Axis Theorem (Baraff, 1989; Gottschalk et al., 1996). This technique is generic for rigid bodies defined as convex polyhedral, and particularly useful if collisions between objects with arbitrary shapes are expected in a given model. However, in this study, particularly in large scale simulations, the vessels are approximated as ellipses for certain practical reasons that are described in Chapter 4. This approximation in vessel shapes allowed the development of a simpler and faster but non-generic algorithm for identifying collisions.

The collision detection algorithm starts with keeping track of the minimum distance between the objects at every time step during the simulation. The minimum distance between two ellipses, which are defined by n points along their boundaries such as $E_1 = \{k_1, k_2, k_3, ..., k_n\}$ and $E_2 = \{l_1, l_2, l_3, ..., l_n\}$, and can be defined as;

$$d_{min}(E_1, E_2) = \min\{d(k_i, l_j)\}, i, j = 1, 2, ..., n$$

where $d(k_i, l_j)$ is the euclidean distance between k_i and l_j . Each point on the boundary of the ellipses is defined in cartesian coordinates as $k_i(x_i, y_i)$ and $l_j(x_j, y_j)$. Also, it must be noted that the cardinality between two ellipses is not a requirement, yet it is assumed here such that to simplify the notation. The collision detection algorithm works in the following steps;

- The minimum distances between all objects are tracked at all time steps.
- If the minimum distance between any two bodies $(d_{min}(E_1, E_2))$ is less than a given tolerance, (ε) , then the bodies are in colliding contact.
- If bodies interpenetrate at time $t_0 + \Delta t$ (Fig. 1b), then the time of collision (t_c) is approximated by evaluating $v_{rel}(t_0)/[d_{min}(t_0) \varepsilon]$. Thus, the time of collision (t_c) should satisfy $t_0 < t_c \le t_0 + \Delta t$.
- Once all the collisions are detected, they are solved in the order of occurrence and the post collision velocities are calculated, as will be discussed in the next section.

2.3.2. Collision solver

Once all the collisions are detected at a given time step and the contact point on each body is identified, the resulting impact force, torque, and velocities of the bodies after the collision are determined.

Fig. 1. a) Ellipses E_1 and E_2 , and the minimum distance, d_{min} between them at time t_0 ; b) Two bodies collide and interpenetration occurs at time $t_0 + \Delta t$; c) The position of the bodies at exact time of collision, t_c , within given distance tolerance of ε.

One common approach for calculating the impact forces is the so-called "penalty" method and is based on the introduction of arbitrary forces (e. g. spring forces) to separate the colliding bodies (Terzopolous et al., 1987). Although this method can generate realistic animations, it is acceptable when the accuracy of the physics is relatively unimportant (Baraff, 1989). The impact force determination can be tackled analytically using the conservation of momentum principle, as will be adopted here. This method has been employed in computer graphics problems widely and is proven to provide physically correct contact forces (Hahn, 1988; Moore and Wilhelms, 1988; Baraff, 1989).

If the two bodies, body A and body B, are in contact at point p, then a given point on body A denoted by $p_a(t)$ should satisfy $p_a(t_0) = p$ at the time of the contact, t_0 . Similarly, point $p_b(t)$ on body B will coincide $p_b(t_0) = p$ at time t_0 . While, at time t_0 , $p_a(t)$ and $p_b(t)$ will overlap, the velocities of these two points might be very different. By evaluating the velocities of these points, which will be denoted by $\dot{p}_a(t_0)$ and $\dot{p}_b(t_0)$ respectively, we can determine whether these two bodies are approaching, separating or in contact with each other. The point velocities are given as:

$$\dot{p_a}(t_0) = v_a(t_0) + \omega_a(t_0) \times (p_a(t_0) - x_a(t_0))$$
 7

$$\dot{p_b}(t_0) = v_b(t_0) + \omega_b(t_0) \times (p_b(t_0) - x_b(t_0))$$

Where, v_a , v_b , ω_a and ω_b are the linear and angular velocities, and $x_a(t_0)$ and $x_b(t_0)$ are the coordinates of the center of masses of the bodies at the time of the contact. Subsequently, the relative velocity, v_{rel} , of the contact points with respect to each other in the direction of contact can be defined by Eqn. (9).

$$v_{rel} = (\dot{p_a}(t_0) - \dot{p_b}(t_0)) \cdot \overrightarrow{n}(t_0)$$

In the above equation, $\overrightarrow{n}(t_0)$ denotes the normal surface vector, which provides the direction of v_{rel} at the contact point. If v_{rel} is positive, it means that v_{rel} and $\overrightarrow{n}(t_0)$ are in the same direction and the bodies are moving away from each other. Then the contact will diminish at time $t_0 + \Delta t$. Yet, we are concerned about the case when $v_{rel} < 0$, which means that the directions of the v_{rel} and $\overrightarrow{n}(t_0)$ are opposite, and the two bodies are in contact at point p. To avoid an interpenetration, the velocities of body A and body B should change rapidly. To create such a near-discontinuity in body velocities, a contact force of F is exerted on the bodies for a very short instant of time, Δt , which leads to a new quantity called the impulse (J):

$$J = F\Delta t$$
 10

The impulse is a vector quantity with the units of mass times acceleration. Applying an impulse will generate the required nearinstantaneous adjustment in the velocity of a body. Then the effect of J on the linear velocity (ν) of a given rigid body with the mass, M, can be driven simply by using the relation $\Delta \nu = J/M$. The impulse acting at contact point p also creates an impulsive torque of τ_J computed using Eqn. (11):

$$\tau_J = (p_c - x_0(t_0)) \times J \tag{11}$$

Where, p_c is the point of contact and x_0 is the location of the center of gravity of the object at the time of the contact. Likewise, the change in the angular velocity $(\Delta\omega)$ of the body with the yaw moment of inertia of I_{zz} due to the impulsive torque is given by $\Delta\omega = \tau_J/I_{zz}$. Therefore if a collision takes place between two bodies, an impulse and a resulting impulse torque will be applied to prevent them from interpenetrating.

Since the tangential or friction forces are neglected here, the direction of the impulse will be in the normal direction, $\overrightarrow{n}(t_0)$ (Fig. 2a). Thus, the impulse J can be written as;

$$J = j \overrightarrow{n}(t_0)$$
 12

where j is a scalar to be calculated and gives the magnitude of the impulse. The sign convention adopted here lets the impulse J act positively on body A, that is, A is subject to an impulse of $(+j\vec{n}(t_0))$, while an equal but opposite impulse $(-j\vec{n}(t_0))$ is exerted on body B (Fig. 2b). To derive the j by using an empirical law for collisions, the following relations need to be provided first:

$$\dot{p}_a^2(t_0) = v_a^2(t_0) + \omega_a^2(t_0) \times r_a$$
 13

Along with,

$$v_a^2(t_0) = v_a^{-1}(t_0) + \frac{j\vec{n}(t_0)}{M_a}$$

$$\omega_a^2(t_0) = \omega_a^1(t_0) + \frac{r_a \times j \overrightarrow{n}(t_0)}{(I_{zz})_a}$$
 15

where $\dot{p_a}^1(t_0)$ and $\dot{p_a}^2(t_0)$ denote the velocity of the body A before and after the impulse J is applied, respectively, and $r_a = p_c - x_a(t_0)$ is the displacement distance. Also, the pre-collision velocities of body A are denoted with $v_a^1(t_0)$ and $\omega_a^1(t_0)$, and the post-collision velocities are shown by $v_a^2(t_0)$ and $\omega_a^2(t_0)$. Combining Eqns. (13)–(15) yields the following;

$$\dot{p_a}^2(t_0) = \left(v_a^{\ 1}(t_0) + \frac{j \, \vec{n}(t_0)}{M_a}\right) + \left(\omega_a^{\ 1}(t_0) + \frac{r_a \times j \, \vec{n}(t_0)}{(I_{zz})_a}\right) \times r_a$$
 16

$$\vec{p}_a^{\ 2}(t_0) = v_a^{\ 1}(t_0) + \omega_a^{\ 1}(t_0) \times r_a + \frac{\vec{j} \, \vec{n}(t_0)}{M_a} + \left(\frac{r_a \times \vec{j} \, \vec{n}(t_0)}{(I_{zz})_a}\right) \times r_a$$
 17

If we substitute Eqns. (10) and (11) into the above expression, we

$$\dot{p_a}^2(t_0) = \dot{p_a}^1(t_0) + j\left(\frac{\overrightarrow{n}(t_0)}{M_a} + \frac{r_a \times \overrightarrow{n}(t_0)}{(I_{zz})_a}\right) \times r_a$$
 18

$$\vec{p_b}^2(t_0) = \vec{p_b}^1(t_0) - j\left(\frac{\vec{n}'(t_0)}{M_b} + \frac{r_b \times \vec{n}'(t_0)}{(I_{zz})_b}\right) \times r_b$$
 19

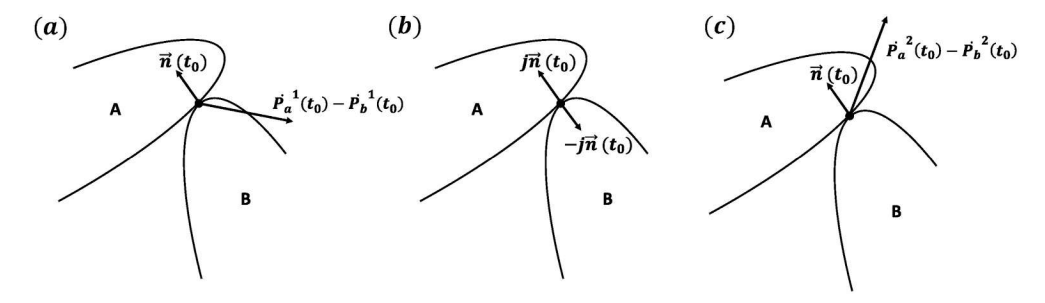


Fig. 2. a) The relative velocity vector at the time of the contact; b) The impulse due to collision acting on each body; c) Post-impulse relative velocity vector.

$$\dot{p_a}^2(t_0) - \dot{p_b}^2(t_0) = \dot{p_a}^1(t_0) - \dot{p_b}^1(t_0) + j\left(\frac{\overrightarrow{n}(t_0)}{M_a} + \frac{\overrightarrow{n}(t_0)}{M_b} + \left(\frac{r_a \times j \overrightarrow{n}(t_0)}{(I_{zz})_a}\right) \times r_a + \left(\frac{r_b \times j \overrightarrow{n}(t_0)}{(I_{zz})_b}\right) \times r_b\right)$$

Following Eqn. (9), we can also introduce v_{rel}^1 and v_{rel}^2 , the pre and post-impact relative velocities in the normal direction:

$$v_{rel}^{1} = (\dot{p_a}^{1}(t_0) - \dot{p_b}^{1}(t_0)) \cdot \overrightarrow{n}(t_0)$$
 21

$$v_{rel}^2 = (\dot{p_a}^2(t_0) - \dot{p_b}^2(t_0)) \cdot \overrightarrow{n}(t_0)$$
 22

$$v_{rel}^2 = -\varepsilon v_{rel}^1$$
 23

where ε is the coefficient of restitution and ranges from 0 to 1. The upper limit, $\varepsilon=1$, yields $v_{rel}^2=-v_{rel}^1$ which means the entire kinetic energy of the system has been preserved and the collision is perfectly elastic. If $\varepsilon=0$, then $v_{rel}^2=0$, indicating a fully inelastic collision in which bodies will stick to each other after the collision.

If we rewrite Eqn. (23) in terms of v_{rel}^1 , v_{rel}^2 and j, and rearrange, then the expression to compute the impulse j becomes;

$$j = -\frac{-(1+\varepsilon)v_{rel}^{1}}{\left(\frac{1}{M_{a}} + \frac{1}{M_{b}} + \overrightarrow{n}(t_{0}) \cdot \left(\frac{r_{a} \times \overrightarrow{n}(t_{0})}{(l_{tz})_{a}}\right) \times r_{a} + \overrightarrow{n}(t_{0}) \cdot \left(\frac{r_{b} \times \overrightarrow{n}(t_{0})}{(l_{tz})_{b}}\right) \times r_{b}}\right)}$$
24

In which M_a , M_b are the masses and $(I_{zz})_a$ and $(I_{zz})_b$ are the yaw moment of inertias of the two colliding bodies. In the case where the body collides into a non-movable body like a berth, wharf or another port infrastructure, the terms with subscript b will vanish in Eqn. (24) since the mass and the inertia of an object that cannot be moved is infinitely large relative to the colliding body. Therefore, for this type of collision, Eqn. (24) simplifies into Eqn. (25):

$$j = -\frac{-(1+\varepsilon)v_{rel}^1}{\left(\frac{1}{M_a} + \overrightarrow{n}(t_0) \cdot \left(\frac{r_a \times \overrightarrow{n}(t_0)}{(t_{lz})_a}\right) \times r_a\right)}$$
 25

Once the impact force, j, is determined, the post-collision velocities, u, v and ω , for each body involved in the collision can be calculated using Eqns. (14) and (15).

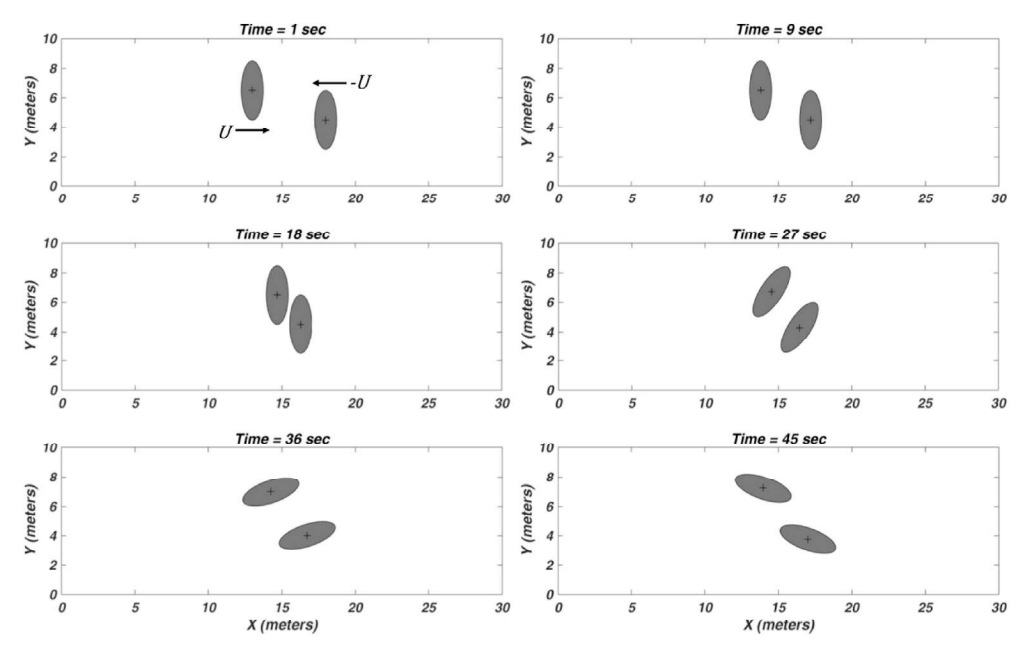


Fig. 3. Time lapse of the eccentric collision takes place between two bodies with equal masses.

To validate the ability of the collision model, various benchmark experiments were produced and example snapshots of a selected case is shown in Fig. 3. During this test it was assumed that the collisions were perfectly elastic. The case given in Fig. 3 was an eccentric collision that included two bodies with equal masses approaching to each other with velocities of equal magnitude of $0.1\,m/s$. Post collision velocities are calculated as $U_1=-0.0317\,m/sec,~V_1=0.0279\,m/sec,~\omega_1=-4.512\,rad/sec$ for the body approaching from left and $U_2=-0.0316\,m/sec,~V_2=0.0282\,m/sec,~\omega_2=-4.546\,rad/sec$ for the one the right, which are consistent with the results obtained from theoretical equations of conservation of momentum.

The second test was based on the work of Gondret et al. (2002), where they experimentally investigated the bouncing motion of spheres in different fluids. In one of their tests, they threw a Teflon sphere with a radius of $3 \, mm$ and a density of $2.15 \, x \, 10^3 \, kg/m^3$ into a 10 cm x 10 cm x 30 cm glass tank filled with air and record its trajectory along with its velocity in time. They use a micropump to release the sphere, which induces an initial velocity of $-0.58 \, m/sec$. During their tests they had not observed significant rotation with this device when releasing the spheres. They also reported that the air friction has negligible impact and the measured coefficient of restitution (i.e. e in Equations (24) and (25)) was 0.80 ± 0.02 and almost remained the same after every bounce. We simulated their experiment with our model, and comparisons of the sphere trajectory and velocity in time are presented in Fig. 4a and b. As indicated by these figures the developed collision model can reproduce the recorded trajectory as well as the post collision velocities perfectly for the entire duration of the experiment both spatially and temporally. Overall, the model's performance in this experiment along with our own tests based on the idealized collisions was exceptional and verified the validity of the collision model.

2.4. Equations of ship motion

frame O(x,y,z) that may coincide with the origin of the computational grid, and the other is a body-fixed frame $O_0(x_0,y_0,z_0)$, which moves and rotates with the ship. For surface vessels, the most commonly adopted position for the body-fixed frame is on the center of gravity (CG) of the ship, which gives hull symmetry about the x_0 - z_0 plane and approximate symmetry about the y_0 - z_0 plane, while the origin of the z_0 axis is relative to the still water surface (Price and Bishop, 1974). In the standard notation given in SNAME (Society of Naval and Maritime Engineers) (1950) and ITTC (International towing tank Conference) (1975), the variables describing the position and orientation of a ship are defined relative to the inertial (earth-fixed) frame, and the coordinates are noted as $[x\ y\ z]^T$ and $[\phi\ \theta\ \psi]^T$. On the other hand, the linear $[u\ v\ w]^T$ and angular $[p\ q\ r]^T$ velocities, forces $[X\ Y\ Z]^T$ and moments $[K\ M\ N]^T$ are expressed in body-fixed coordinate system.

Here, we can define two vectors, one of which represents the position/orientation (Eqn. (26)) with respect to earth-fixed coordinate system, whilst the other expresses the linear/angular velocities of Eqn. (30) according to the body-fixed frame. Consequently, the rate of change of the position/orientation vector can be obtained using the relation given in Eqn (31).

$$n = [x y z \varphi \theta \psi]^T$$
 26

$$\nu = \left[u \, v \, w \, p \, q \, r \right]^T \tag{27}$$

$$\dot{n} = R(n)\nu \tag{28}$$

where, R(n) is a transformation matrix based on the Euler angles (φ, θ, ψ) given as in (Fossen, 1994):

$$R(n) = \begin{bmatrix} R_1(\varphi, \theta, \psi) & 0_{3x3} \\ 0_{3x3} & R_2(\varphi, \theta, \psi) \end{bmatrix}$$
29

$$R_1(\varphi, \theta, \psi) = \begin{bmatrix} \cos(\psi)\cos(\theta) & -\sin(\psi)\cos(\varphi) + \cos(\psi)\sin(\theta)\sin(\varphi) & \sin(\psi)\sin(\varphi) + \cos(\psi)\cos(\varphi)\sin(\theta) \\ \sin(\psi)\cos(\theta) & \cos(\psi)\cos(\varphi) + \sin(\varphi)\sin(\theta)\sin(\psi) & -\cos(\psi)\sin(\varphi) + \sin(\theta)\sin(\psi)\cos(\varphi) \\ -\sin(\theta) & \cos(\theta)\sin(\varphi) & \cos(\theta)\cos(\varphi) \end{bmatrix}$$
30

The traditional approach to express ship motion is with two reference frames to define the equations of motion. One is the fixed to earth

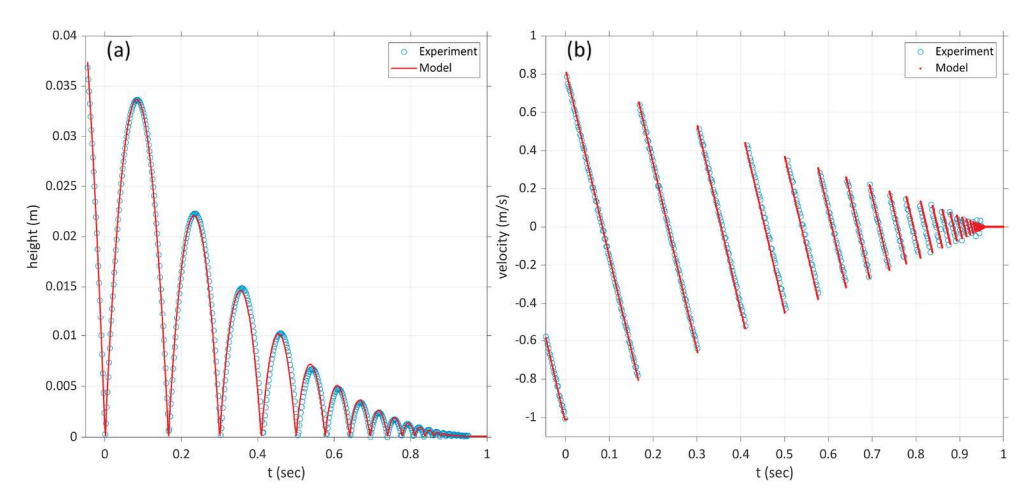


Fig. 4. Time histories of modeled a) sphere trajectory and b) sphere velocity compared to experimental data. Blue hallow circles show the experiment results, whereas red line in (a) and red dots in (b) are model outputs. (For interpretation of the references to colour in this figure legend, the reader is referred to the Web version of this article.)

$$R_2(\varphi, \theta, \psi) = \begin{bmatrix} 1 & \sin(\varphi)\tan(\theta) & \cos(\varphi)\tan(\theta) \\ 0 & \cos(\varphi) & -\sin(\theta) \\ 0 & \sin(\varphi)/\cos(\theta) & \cos(\varphi)/\cos(\theta) \end{bmatrix}$$
 31

Then, following Newton's second law, the equations of motion of the vessel with respect to the body-fixed coordinate system can be written in the vector form as:

$$M\dot{\nu} = F(\dot{\nu}, \nu, n)$$
 32

where M represents the mass and inertia matrix due to the rigid body dynamics, and F is all the forces arising due to flow or the motion of the hull in water. Generally, in comparison to the other motions, pitch and heave are neglected for conventional ships, which leaves us with 4-degrees of freedom (dof); surge, sway, yaw and roll (e.g. Perez and Blanke, 2002; Skejic and Faltinsen, 2008). As an initial assumption, the ship motion is restricted in the horizontal plane, thus, the roll motion is also ignored in this study. Subsequently, the equations of motion in 3-dof (surge, sway, and yaw) are expressed as:

$$m(\dot{u} - vr) = X_{hull} + F_{xc}$$

$$m(\dot{v} + ur) = Y_{hull} + F_{yc}$$

$$I_{zz}\dot{r} = N_{hull} + N_{wave}$$
33

where, m is the mass and I_{zz} is the moment of inertia of the vessel. The external forces acting on the hull due to movement of the vessel and the flow passing through will be described in more detail below.

The hull forces are the sum of all the hydrodynamic forces exerted on the hull. They are also called the hydrodynamic derivatives and appear in the series expansion of the hull forces;

$$X_{hull} \cong X_u \dot{u} + X_{uu} u^2 + X_{r|u|} r|u| + \dots$$
 34

where

$$X_{ii} = \frac{\partial f_X}{\partial u^i}, \quad X_{uu} = \frac{\partial^2 f_X}{\partial u^2}, \quad X_{r|u|} = \frac{\partial^2 f_X}{\partial r \partial |u|}$$

The above coefficients represent a different component of the inertia forces. For instance, X_{ii} means the force in x_0 -direction due to the acceleration \dot{u} in x_o -direction and so forth. But due to blind expansion of the series, higher order non-linear derivatives do also appear, and the basic difficulty in this type of analysis is to determine the values of these nonlinear coefficients for each hull shape and vessel type (Morgan, 1978). Following Newton's second law which states that the hull forces depend linearly on the acceleration only, we retain the first order acceleration terms, and neglect the cross derivatives including both velocities and accelerations (Fossen, 1994). Consequently, in this study, only the linear inertia terms are kept. The first terms are the added mass and inertia terms arising due to the motion of the fluid associated with the accelerations produced by the ship, which also reflects the build-up of the kinetic energy of the fluid as the hull moves. Furthermore, the first order viscous damping terms are also important, especially in the case of free motions, where the vessel drifts (Bandyk and Beck, 2009). The resulting equations of motion are:

$$X_{hull} = -X_{\dot{u}}\dot{u} + Y_{\dot{v}}vr + X_{\dot{v}}vr$$

$$Y_{hull} = -Y_{\dot{v}}v - X_{\dot{u}}ur$$

$$N_{hull} = -N_{\dot{r}}\dot{r}$$
35

In the above equation, the terms with coefficients X_{ii} , $Y_{i'}$ and N_{f} are the forces due to added mass and inertia. Some common methods in estimating these hydrodynamic parameters include CFD modeling or running controlled laboratory experiments and deriving the coefficients by the analysis of the acquired data (Blanke and Jansen, 1997). If Equations (33) and (35) are merged and arranged, they can be expressed in the matrix form as $A \cdot \dot{U} = b$, where the matrix and the vectors are;

$$\begin{bmatrix} m + X_{ii} & 0 & 0 \\ 0 & m + Y_{ij} & 0 \\ 0 & 0 & I_{zz} + N_{\dot{r}} \end{bmatrix} \begin{bmatrix} \dot{u} \\ \dot{v} \\ \dot{r} \end{bmatrix} = \begin{bmatrix} (m + Y_{\dot{v}} + X_{vr})vr + F_{xc} \\ -(m + X_{ii})ur + F_{yc} \\ N_{wave} \end{bmatrix}$$
 36

 F_{xc} and F_{yc} are the external forces due to flow and they are calculated using empirical relations, and N_{wave} is the torque generated by F_{xc} and F_{yc} . The governing equations to determine the transverse and longitudinal forces arising from the tsunami currents on vessels are acquired from U.S. Army Corps of Engineers report (2005) on mooring line design guidelines. The approach is intended to be first order, and thus differential loads are not treated in this phase of the analysis. These equations have also been employed by Keen et al. (2017) and found to be sufficient tsunami load estimates. The static transverse drag force, F_{yc} acting on the vessel is calculated using;

$$F_{yc} = 0.5 \, \rho_w \, L_{wL} \, T \, C_{yc} \, V_c \, |V_c| \sin(\theta_c)$$
 37

Where, F_{yc} = Transverse current force (N); ρ_w = mass density of water (kg/m^3) , V_c = current velocity (m/s), L_{wL} = vessel waterline length (m); T = average vessel draft (m); C_{yc} = transverse current force drag coefficient and θ_c = incident current angle (degrees). The drag coefficient, C_{yc} which includes the effects of water depth and vessel's underkeel is given by;

$$C_{yc} = C_0 + (C_1 - C_0) \left(\frac{T}{d}\right)^2$$
 38

In Eqn. (38), d is the water depth, C_1 is shallow water current force drag coefficient with the recommended value of 3.2 ($C_1 = 3.2$). The deep water drag coefficient, C_0 , can be obtained by;

$$C_0 = 0.22 \sqrt{X}$$
 39

$$X = L_{wL}^2 \frac{A_m}{R V}$$

where, X = dimensionless ship parameter; $A_m =$ immersed cross-sectional area of the ship midsection (m^2) ; B = beam of the vessel; V = submerged volume of the ship (m^3) .

Unlike transverse loads, the order of magnitude of the skin friction competes with the longitudinal form drag for streamlined vessels. Therefore, both types of drag forces have to be considered while calculating the total static longitudinal current forces. Neglecting the propeller forces, the longitudinal drag is given by;

$$F_{xc} = F_{xFORM} + F_{xFRIC} \tag{41}$$

where

$$F_{xFORM} = 0.5 \rho_w B T C_{xcb} V_c |V_c| \cos \theta_c$$

$$F_{xFRIC} = 0.5 \rho_w S C_{xca} V_c |V_c| cos\theta_c$$
43

In Eqns. (42) and (43); C_{xcb} is longitudinal current form drag coefficient and equals to 1 ($C_{xcb} = 1$), and C_{xca} and S are the longitudinal skin friction coefficient and wetted surface area (m^2) respectively. Here these parameters are estimated using;

$$S = 1.7 T L_{wL} + \frac{D}{T \gamma_w}$$
 44

$$C_{xca} = 0.075 / [(\log_{10}R_N) - 2]^2$$
 45

where, γ_w is specific weight of water and R_N is the Reynolds number, and for vessels it is computed using Eqn. (46);

$$R_N = \frac{\left| V_c L_{wL} \cos(\theta_c) \right|}{\nu}$$
 46

Finally, the yaw moment N_{wave} , can be calculated as the sum of the torque created due to eccentricity (x', y') of the lateral and longitudinal drag forces:

$$N_{wave} = F_{xc}y' + F_{yc}x'$$
 47

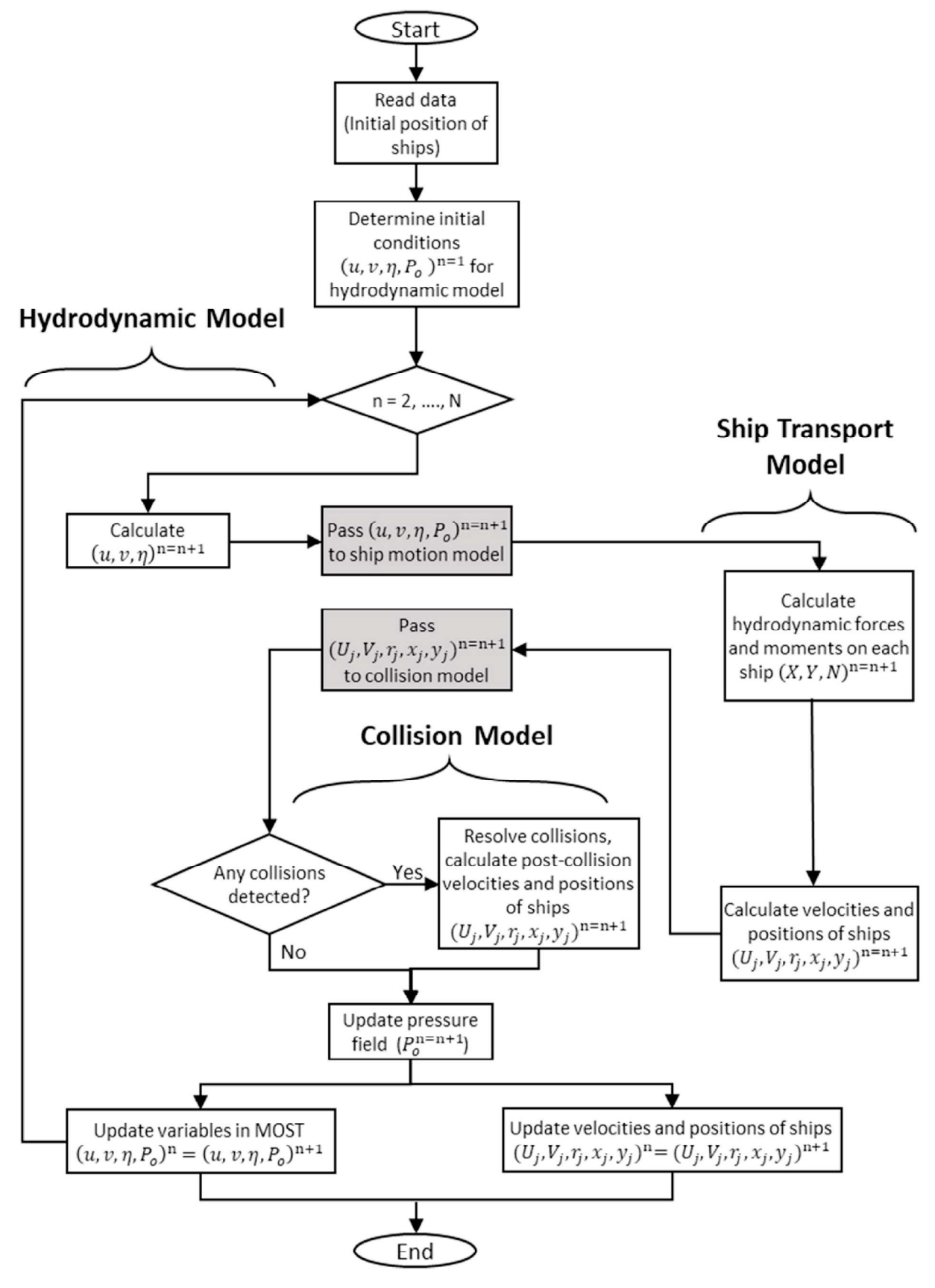


Fig. 5. The workflow of the coupled model.

2.4.1. Time integration method

Equation of ship motion (Eq. (36)) is discretized using first order, explicit Euler Method, as given in Eq. (51),

$$u^{n+1} = u^{n} + \frac{\Delta t}{(m+X_{ij})} \left[(m+Y_{ij} + X_{vr})vr + F_{xc} \right]$$

$$v^{n+1} = v^{n} + \frac{\Delta t}{(m+Y_{ij})} \left[-(m+X_{ii})ur + F_{yc} \right]$$

$$r^{n+1} = r^{n} + \frac{\Delta t}{(I_{zz} + N_{ij})} N_{wave}$$
48

Once the new velocities (i.e. u^{n+1} , v^{n+1} , r^{n+1})at the next time step are obtained, position of ships in global coordinates updated using again Euler method.

2.5. Workflow of the coupled model

The overall procedure followed by the coupled model is outlined below and summarized in the flowchart shown in Fig. 5. Assuming that all the dependent variables $(u, v, \eta, P_o, U_j, V_j, x_j, y_j)$ in the hydrodynamic model and ship transport model are known at $t = t_n$;

- 1 Calculate the free surface elevation (η) and depth-averaged flow velocities (u, v) at $t = t_{n+1}$ in the hydrodynamic model.
- 2 Pass u, v, η to ship transport model to calculate hydrodynamic forces and moments, and surge (U_j) , sway (V_j) velocities along with the rate of yaw (r_j) for each ship subsequently. Then update position of each ship (x_i, y_i) temporarily for $t = t_{n+1}$.
- 3 Pass $(U_j, V_j, r_j, x_j, y_j)$ to the collision model and search for any collisions that occurred either between ships or ships and land.
- 4 If there are not any collisions detected, then skip to step 6.
- 5 If collisions are detected sort them in order of occurrence and calculate impact forces. Calculate variables for each ship using impact forces from step 3 at $t = t_{n+1}$.
- 6 Update the pressure field (P_o) at $t = t_{n+1}$.
- 7 Update all the dependent variables in hydrodynamic and ship transport models.
- 8 Return step 1 and repeat the procedure for the next time step.

3. Validation of MOST

3.1. Advancing moving pressure disturbance

The wave train created by a traveling ship consists of a long leading

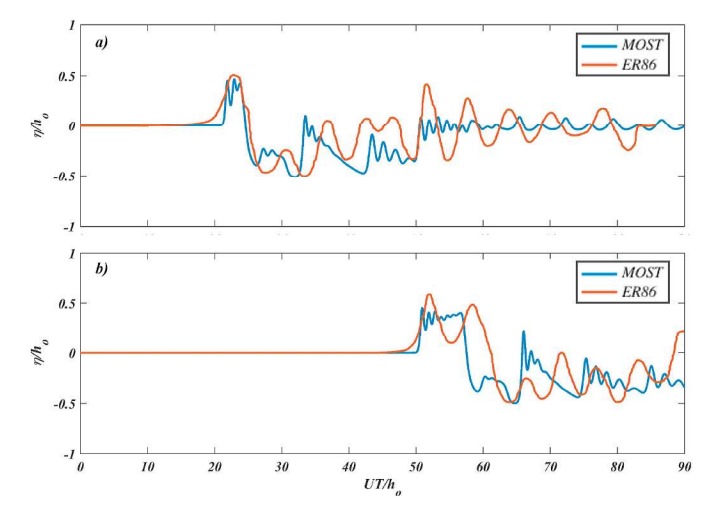


Fig. 6. Comparison of free surface elevations calculated in MOST with ER86's model at a) $65h_o$ and b) $130h_o$ ahead of the initial position of the pressure disturbance for $\bar{p}=0.3$ and Fr=1.0 according to the formulation of ER86.

bow wave and a trailing long hull wave, and a series of diverging waves in between. Physically, these diverging waves are short and dispersive; note that the nonlinear shallow water equations, with their lack of the relevant dispersion terms, cannot produce the free surface generated by the ship where dispersion is important. Hence, only the leading bow wave in front and the stern wave behind the vessel can be produced adequately by an NSW model like the one employed in this study. However, the main purpose of this study, as mentioned earlier, is to capture features such as the acceleration/deceleration/eddies generated due to flow interaction with the ship hull, rather than focusing on the waves generated by vessels. Nonetheless, to assess the model's performance in producing the leading bow wave and thus the general process of flow-vessel interaction, our model results are compared to numerical results published in Ertekin et al. (1986) (ER86 hereafter). ER86 presents a numerical method to solve dispersive, rotational, inviscid Green-Naghdi equations (Green and Naghdi, 1976) in three dimensions to model the solitons preceding moving disturbances (e.g. ships) in long basins. ER86 presents results from tests conducted for Froude numbers of 0.7, 0.9, 1 and 1.2. They observed that solitons were generated in cases when Fr < 1.2 traveling upstream faster than the moving pressure

A quantitative evaluation of the present model performance with respect to ER86 model is given in Fig. 6, in which free surface elevations generated by MOST are compared to ER86 data for a disturbance moving upstream at critical velocity, i.e., Fr = 1. From Fig. 6a, it can be seen that the leading crest produced by MOST provides good agreement with ER86 results. Both the wave amplitude and the phase are captured reasonably well. However, MOST results, with the first trough, start to show phase errors and diverge from ER86 data. This difference is particularly clear after the second wave and can be attributed to the lack of dispersion and numerical breaking in MOST. Free surface elevations are further compared at a later time for the same case in Fig. 6b. Although it can be argued that the crest elevations of the leading waves look similar, the wave profiles are significantly different. In ER86 data, it is apparent that the solitons are formed and separated from the pressure disturbance, whereas in MOST, the leading crest gets longer and with a steep breaking front. There is waviness in the depression region in both models, but the profiles do not match. This difference is somewhat expected due to the high nonlinearity of the leading wave in ER86 model. as the ratio of wave amplitude (a) to water depth (h_0) is around 0.5 (Dean and Dalrymple, 1991), which can be handled numerically by a fully nonlinear dispersive model, whereas the leading solitary wave is transformed into a breaking bore in the non-dispersive MOST simulation. On the other hand, Lee et al. (1989) state that during their laboratory experiments they also have observed breaking of the leading waves when the peak pressure (variable p_{max} according to the formulation of ER86) of the disturbance was greater than 0.15, although the numerical results in ER86 do not indicate that. Here, we must note that the main purpose of this exercise is to assess whether the pressure gradient terms are implemented correctly within the numerical stencil of MOST. Therefore, we are not concerned about the discrepancy between ER86 and our model that appears at the later stages of the simulation (Fig. 6b) as the aim of this study is not to model ship generated waves.

3.2. Benchmark case in OpenFOAM

A benchmark test was set-up using an open source CFD software, OpenFOAM, to assess the proposed model's ability to generate the wake field behind a floating object for an idealized and simplified case. As OpenFOAM retains numerous solvers that can address a wide variety of CFD problems, IHFOAM was selected to be used for this benchmark problem. IHFOAM is a two-phase, incompressible fluid solver based on the Reynolds Averaged Navier-Stokes (RANS) equations using the volume of fluid (VoF) method and offers realistic wave generation and absorption boundary conditions (Higuera et al., 2014). The governing

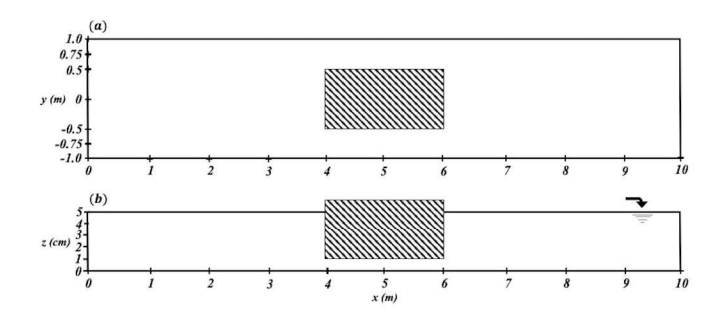


Fig. 7. Schematic view of the OpenFOAM benchmark set-up. a) Top-view, b) Side view of the set-up (vertically exaggerated).

equations of IHFOAM are given by;

$$\frac{\partial \widetilde{u}_i}{\partial x_i} = 0 \tag{49}$$

$$\frac{\partial \rho \widetilde{u}_{i}}{\partial x_{i}} + \widetilde{u}_{j} \frac{\partial \rho \widetilde{u}_{i}}{\partial x_{i}} = -g_{i} x_{j} \frac{\partial \rho}{\partial x_{j}} + \mu_{eff} \frac{\partial}{\partial x_{j}} \left(\frac{\partial \widetilde{u}_{i}}{\partial x_{j}} \right) + \frac{\partial \rho}{\partial x_{i}}$$
50

where \widetilde{u}_i is the velocity vector (i.e $\widetilde{u}_i = (u, v, w)$), g is the gravitation acceleration and p is the dynamic (excess) pressure. Additionally, μ_{eff} is the effective coefficient of viscosity, which combines the effects of dynamic molecular viscosity and viscous diffusion and/or dissipation due to turbulence in the flow $(\mu_{eff} = \mu + \rho \nu_{turb})$. The dynamic viscosity of water is, $\mu = 1e - 3 \text{ kg/m} \cdot \text{s}$, while the additional viscosity due to turbulence, ν_{turb} , is estimated based on the selected turbulence model in OpenFOAM; here we use a k-ω SST model (Menter, 1994). This second order diffusion/dissipation term is one of the key differences between OpenFOAM and MOST when it comes to physics included in the untheory of the models. In simulations turbulence-controlled features such as large eddies and wakes are generated in the flow, the significance of these terms gets large (Kim et al., 2009). Therefore, OpenFOAM is expected to provide results closer to reality and sets a practical benchmark to assess the performance of MOST following the modifications made to include vessels into calculations.

The test was conducted in a 10-m-long and 2-m-wide shallow tank, where a floating block is placed in the center of the channel (Fig. 7). The block does not move from its initial location. A steady upstream flow discharged into the tank, where the water is initially at rest, with a depth-averaged velocity (*U*) of 0.1 m/s. The water depth (h_0) in the tank was 0.05 m, which translates into $Re \approx 50000 \; (Re = UL/\nu)$, where L is the distance from edge of the block to tank wall, 0.5 m) and $Fr \approx$ $0.15 \ (Fr = U/\sqrt{gh_0})$. The floating block was 2 m in length and 1 m wide, with a draft of 0.04 m. The draft to water depth ratio (D/h_o) of the block is 0.8. Since the block remains immersed during the entire simulation, the generated wake in MOST was generated through gradients in the pressure and stress. To account for the skin friction shear of the block, a Manning's n value of 0.12 was used at the block, compared to a value of 0.03 away from the block. Last but not least, the velocities predicted by OpenFOAM is also depth-averaged across the vertical layers to be consistent with MOST outputs. Uniform inflow condition along with the geometry used are intentionally specified rather simplistic to better assess the influence of modifications made to MOST. Even with this simple setup, flow gets quite complex due to rapidly varying flow speed as it passes the object. Additionally, the wake region generated behind the object is driven by the flow passing from both sides as well as under the block. These conditions do also lead to a vertical mixing layer, which further contributes to the complexity of the flow state in the lee side of the object.

The vorticity $(\omega_z = \nabla \ \times \ \textbf{u})$ field maps and swirl strength (λ_{ci}) of the

vortices are compared in Fig. 9 and Fig. 9 respectively. Swirl strength conveys the local frequency of the rotation $(T = 2\pi/\lambda_{ci})$ and can be calculated for the vortices that experience swirling motion by using the local velocity gradient tensor given in 9.

$$\mathbf{D}^{2D} = \begin{bmatrix} \frac{\partial u}{\partial x} & \frac{\partial u}{\partial y} \\ \frac{\partial v}{\partial x} & \frac{\partial v}{\partial y} \end{bmatrix}$$
 51

The tensor given in Eqn. (9) has either two real eigenvalues or pair of complex conjugate eigenvalues (Adrian et al., 2000). The swirl strength, λ_{ci} , is zero unless the vortex undergoes swirling motion, otherwise λ_{ci} is equal to the imaginary part of the complex conjugate pair. The difference between vorticity and the swirl strength is that the shear layers are excluded in the latter, so the boundaries defined by the $\lambda_{ci} = 0$ contain only the core of the vortex (Adrian et al., 2000).

From Figs. 8 and 9, it can be seen that at early times, models show similar behavior. The flow starts to separate from the right and left tips of the block at around t = 10 s. The separation regions grow as the flow supplies momentum through the gaps at the sides of the block. Two symmetric eddies with positive and negative vorticities are generated on the right and the left corners, respectively, of the block. MOST captures the generation of the eddies well at this initial stage when compared to OpenFOAM. As the flow progresses, the eddies are carried away from the block until they detach by t = 20 s. As vortices are advected downstream, after t = 20 s, the energy becomes more concentrated near the channel center in MOST, whereas the energy is more diffused in OpenFOAM. This becomes more apparent as time evolves, and the vortices in OpenFOAM spread in space faster than their counterparts in MOST. Also, smaller eddies appear starting from $t \approx 30 \, s$ in MOST, which don't merge with the main vortices and spread towards the downstream in an erratic fashion. These differences are most readily attributed to lesser eddy diffusion away from the block in MOST as compared to OpenFOAM.

In OpenFOAM, the structure of the eddies is more consistent (less high wavenumber energy), while their energy consistently decays due to viscous dissipation until the end of the simulation. This major and main difference among the two models is expressed distinctly in Fig. 10, where maximum vorticity fields from MOST and OpenFOAM simulations as well as the absolute $(abs(\omega_{MOST} - \omega_{OpenFOAM}))$ and relative $((\omega_{MOST} - \omega_{OpenFOAM})/\omega_{OpenFOAM} \times 100)$ differences of two are plotted. In MOST the maximum vorticity is mainly confined in the area marked by the red dashed lines in Fig. 10a. The boundaries of this region defined by the smaller eddies traveling downstream, in fact, their streaks are conspicuous in Fig. 10a. On the other hand, the maximum vorticity field from OpenFOAM postulates a more homogenous behavior (Fig. 10b), and vortices eventually expand into the entire downstream region, beyond the red dashed lines. That is why the relative difference in maximum vorticities (Fig. 10d) is always negative and goes up -100%outside of the red lines, contrary to inside. When we evaluate the difference in vorticity field between two, in absolute terms, it ranges from ± 0.2 (1/s) to ± 1.0 (1/s) locally (Fig. 10c), but the range of the relative difference is more significant and goes up to 100% at some locations as can be seen in Fig. 10d. Inside the area enclosed by the black polygons, where the wake region behind the object mainly develops, there is a hotspot at $x \approx 6.5$ m Fig. 10d. This hotspot occurs where the cores of the main vortices in MOST settle and it is completely expected considering the fact that the energy is concentrated mainly in the center of these as opposed to their counterparts in OpenFOAM (Fig. 8) and leading to the substantial difference in maximum vorticities being observed here. Yet, the rest of the area inside the black polygons experiences a relative difference $\pm 25\%$. Some other local high discrepancy regions arise after x = 7 m due to smaller eddies converging into the centerline.

Lastly, we use the circulation growth of the vortices as a metric to compare the two models (Fig. 11). The circulation corresponds to the

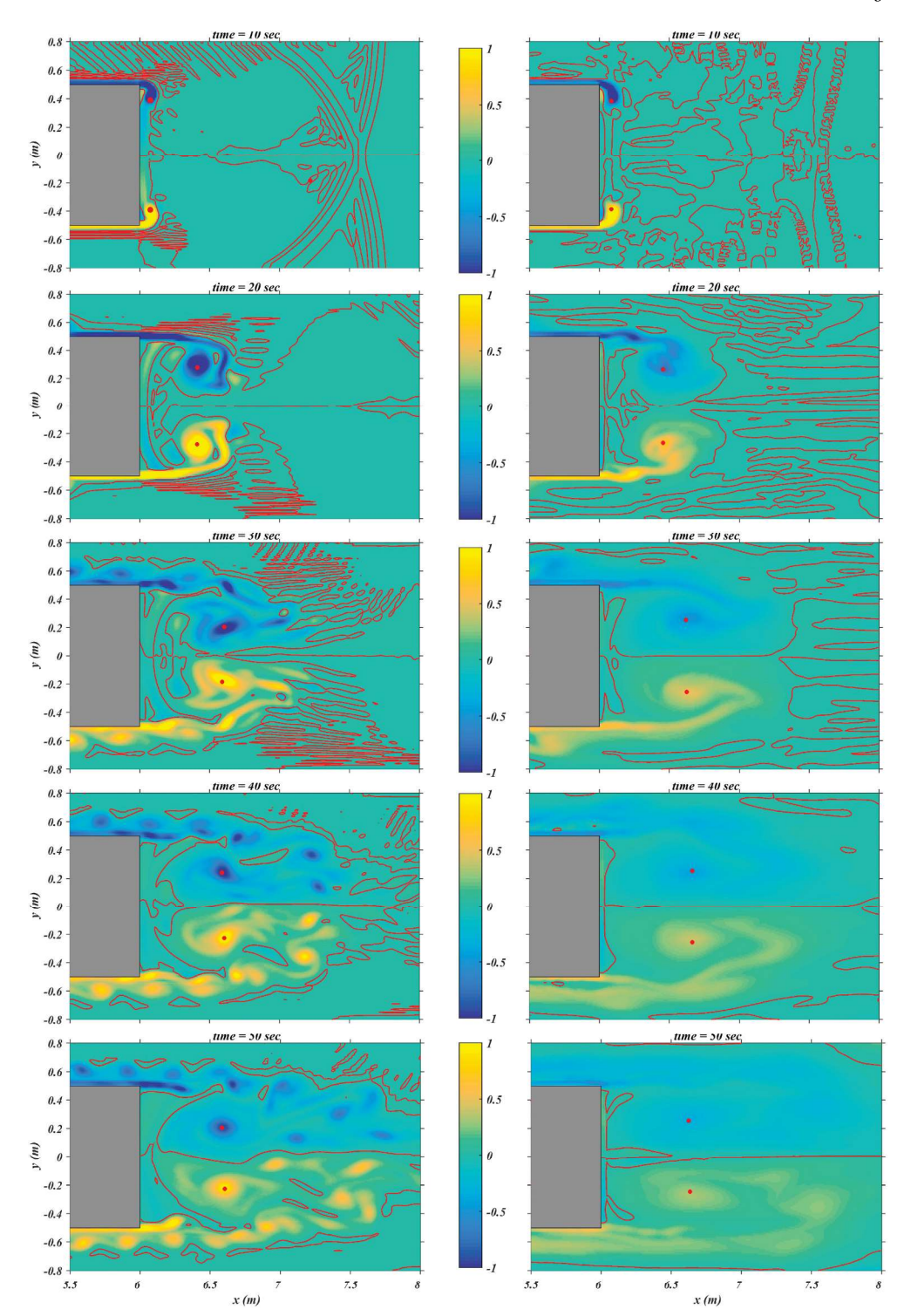


Fig. 8. Vorticity (ω_z) maps at various times during vortex generation and evolution. The red lines represent the $\omega_z=0$ contour. Left panel MOST; right panel OpenFOAM results. (For interpretation of the references to colour in this figure legend, the reader is referred to the Web version of this article.)

sum of the vorticity in an enclosed surface, *S*, and can be approximated as the discrete sum of the vorticity of each cell inside the surface (Mimeau and Mortavazi, 2021; Krueger, 2005).

$$\Gamma_{vortex} = \iint \omega_z dS \approx dx dy \sum_{i=1}^{N} \sum_{j=1}^{M} \omega_{i,j} \quad (x_j, y_i)_{i=1:N} = \sum_{j=1:M} \sum_{j=1:M} (x_j, y_j)_{j=1:M}$$
52

The total circulation is evaluated only inside the domain enclosed by the blue polygon shown in Fig. 11a due to axisymmetric flow, and the circulation growth in both models is compared in Fig. 11b. The rate of circulation growth in both models is consistent until $t \approx 30 \, s$, indicating that MOST can produce the same amount of vorticity as in OpenFOAM, which is also evident in Fig. 8, despite spatial differences. However, the circulation growth starts to slow down after this time in MOST, particularly due to smaller eddies leaving the blue polygon. Conversely, in OpenFOAM total circulation keeps growing steadily until $t \approx 50 \, s$, until the circulation supply ends. By then, the vortices already cover a broad area than the ones in MOST, beyond the red dashed lines shown in

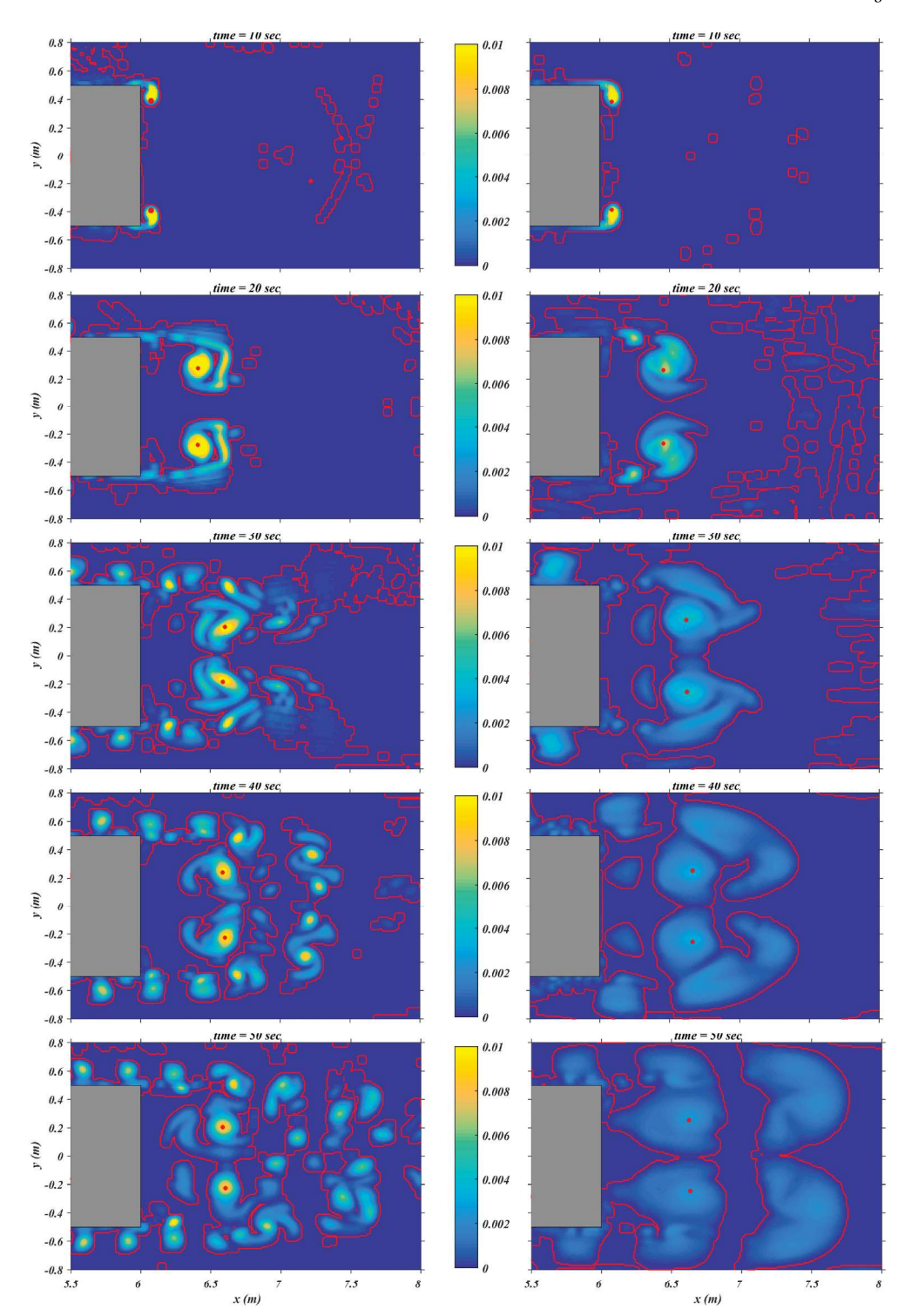


Fig. 9. Swirl strength (λ_{ci}) maps at various times during vortex generation and evolution. The red lines represent the $\lambda_{ci}=0$ contour. Left panel MOST; right panel OpenFOAM results. (For interpretation of the references to colour in this figure legend, the reader is referred to the Web version of this article.)

Fig. 10b. Lastly, if we take a look at the amount maximum total circulation reached during the simulation in each model is compared, it is about 20 % less in MOST than OpenFOAM (0.150 m^2/s and 0.185 m^2/s respectively).

The difference in the coherence and the growth of the vortices observed between the two models can be explained by the lack of a viscous turbulence model in MOST that provides horizontal and vertical mixing. Therefore, MOST cannot generate a stable wake region in this scale after about the midpoint of the simulations. However, despite these

differences, given the limitations of MOST due to its relatively simple shallow water wave theory, these comparisons show its' ability to provide reasonable realization for energetic flow passing a floating object in a computationally cheaper way. Additionally, it is found that the impact of these differences is subtle in the geophysical scale (Lynett et al., 2014).

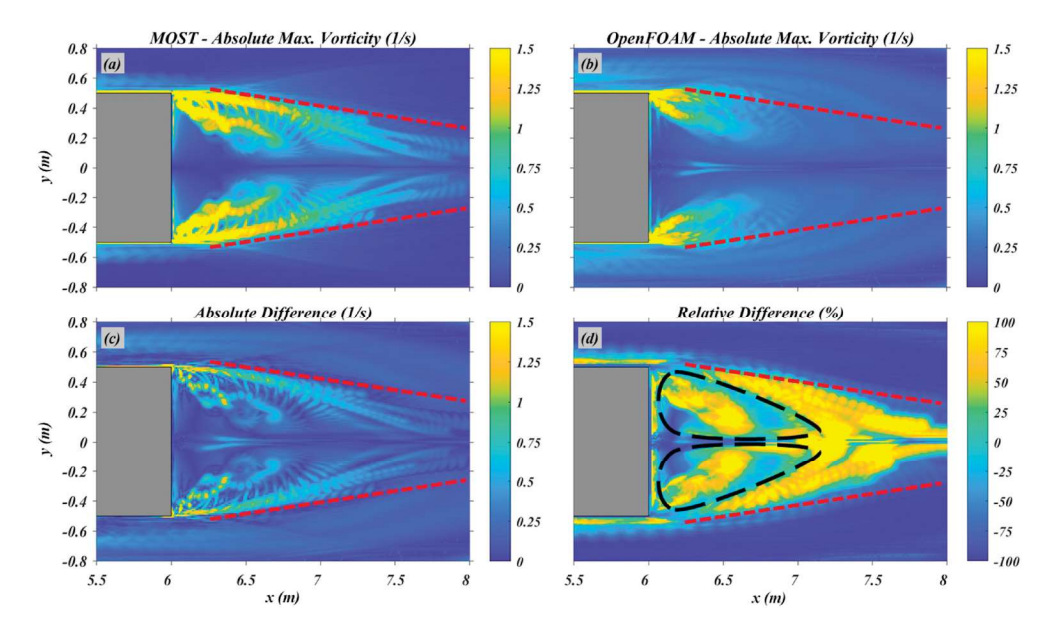


Fig. 10. a) Maximum absolute vorticity field predicted by MOST and b) by OpenFOAM after a 60-s-long simulation, c) absolute difference of the vorticity fields between MOST and OpenFOAM, and d) relative difference (%) between MOST and OpenFOAM.

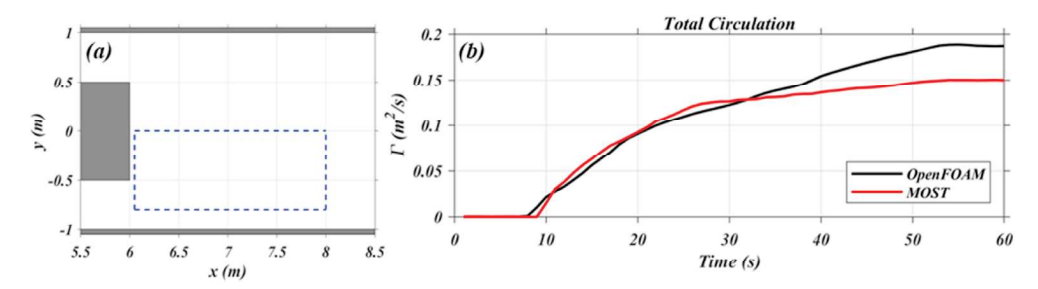


Fig. 11. a) blue polygon shown in the figure confines the area over which the total circulation evaluated b) the comparison of the circulation growth of the vortices generated in MOST and OpenFOAM. (For interpretation of the references to colour in this figure legend, the reader is referred to the Web version of this article.)

4. Results and discussion of large scale applications

The developed model was tested in two locations for two different tsunamis. In the first test, the effects of a hypothetical tsunami arising from Alaska-Aleutians Subduction Zone was investigated for the ships moored in Port of Long Beach. The purpose of this analysis was to see if the presence of vessels within the port changes the flow field created by the tsunami, and if so, does the variation intensify as the number of the ships in and around the terminal increases? Then, another experiment was conducted based on the post-tsunami data collected after the 2011 Tohoku Tsunami in Port of Ishinomaki, Japan. Based on a personal communication with Japanese researchers in April 2018, it has been found out that a container ship broke free off its' moorings and was pulled out of the terminal by the currents during the event. A realization of this event was made using the developed transport model based on the best estimates of the vessel's draft, location and release time at the time of the incident. However, the values of these parameters cannot be known precisely before the incident. Therefore, a sensitivity analysis was also performed based on this case to see the effects of the initial choice of these parameters on the predicted behavior of the vessel.

In these experiments, the ships were approximated as ellipses, and the pressure disturbances therefore were defined as elliptic gaussian functions given by Eqn. (53). The coefficients c_1 , c_2 and c_3 are the shape parameters that define the width and the length of the gaussian, as well as the ship's alignment with respect to earth fixed coordinate system based on the angle of rotation, θ .

$$Z(x,y) = A*\exp\left[-\left(c_1(X-x0)^2 + 2c_2(X-x0)(Y-y0) + c_3(Y-y0)^2\right)\right]$$
 53

where;

$$c_{1} = \frac{\cos(\theta)^{2}}{\left(2\sigma_{x}^{2}\right)} + \frac{\sin(\theta)^{2}}{\left(2\sigma_{y}^{2}\right)}, c_{2} = -\frac{\sin(2\theta)}{\left(4\sigma_{x}^{2}\right)} + \frac{\sin(2\theta)}{\left(4\sigma_{y}^{2}\right)}, c_{3} = \frac{\sin(\theta)^{2}}{\left(2\sigma_{x}^{2}\right)} + \frac{\cos(\theta)^{2}}{\left(2\sigma_{y}^{2}\right)}$$

4.1. Hypothetical tsunami scenario in Port of Long Beach

The Alaska-Aleutians Subduction Zone (AASZ) is one of the most threating far-field tsunami source regions for California. In recent history, there had been three remarkable tsunamigenic earthquakes: the 8.2 Mw 1946 Aleutian Islands (Johnson and Satake, 1997), 8.6 Mw 1957 Andreanof Islands (Johnson et al., 1994) and 9.2 Mw 1964 Prince William Sound (Kanamori, 1970) earthquakes. Each of these earthquakes were followed by tsunamis in the Pacific which all impacted California. More recently, tsunami hazard assessment study of Kalligeris et al. (2017) showed that AASZ poses the greatest tsunami hazard potential

Table 1The main parameters of the vessels used in Port of Long Beach simulations.

Length	Meters	300
Beam	Meters	60
Draft	Meters	10
Deadweight	Tons	150,000
Displacement	Cubic meters	120,000

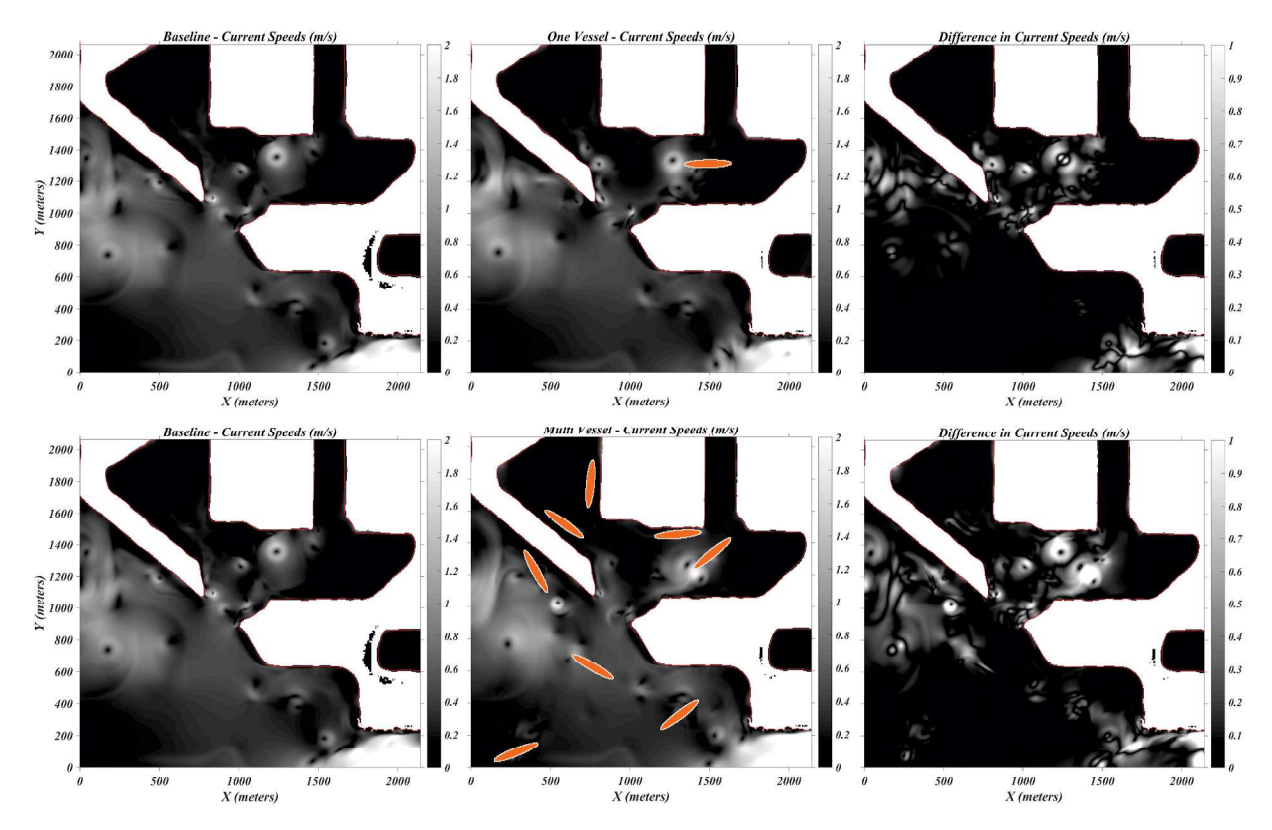


Fig. 12. Current speeds extracted 100 min after the arrival of the first wave. Right panel shows the current field from the baseline simulation; middle panel are the current speeds when vessels are included; right panel absolute difference of current speeds predicted in both cases. The figures on top are from one-ship simulation, while the bottom plots are from the multi-ship case.

for California among all the subduction zones along the Pacific Rim.

The source characteristics of the hypothetical tsunami scenario considered in this study are based on the 1964 earthquake, but it is located to the west of the 1964 rupture to increase the energy beamed towards California. The estimated rupture area is 700 km long and 100 km wide with an average slip of 25 m. Overall, the source corresponds to a magnitude 9.2 earthquake. The details of the earthquake source parameters of this event were given by Barberopoulou et al. (2011).

Based on this tsunami scenario, two different simulations are set-up focusing on the Port of Long Beach. In the first test, only one ship was placed within the port, while the second case had eight identical ships located in and around the port. The parameters of the ships considered in this part of the analysis is given in Table 1. Additionally, the results from these two simulations were compared with a baseline simulation where no ships were present to see the extent of the variations in the flow field induced by the vessels. A nested grid was established for these cases to propagate the tsunami waves from Aleutians-Alaska Subduction Zone to the Port of Long Beach. Here the grid size (Δx) of the innermost computation grid was set to 5 m resolve the vessels sufficiently. In this final level of the nested grids, the simulations were run for 10 h of tsunami action.

The results of these two sets of simulations were compared in Fig. 12 with the plots showing the current speeds estimated 100 min after the first arrival of the tsunami to the port. When only one ship was included, the difference in the flow fields compared to the baseline simulation

Table 2
The main parameters of C.S Victory.

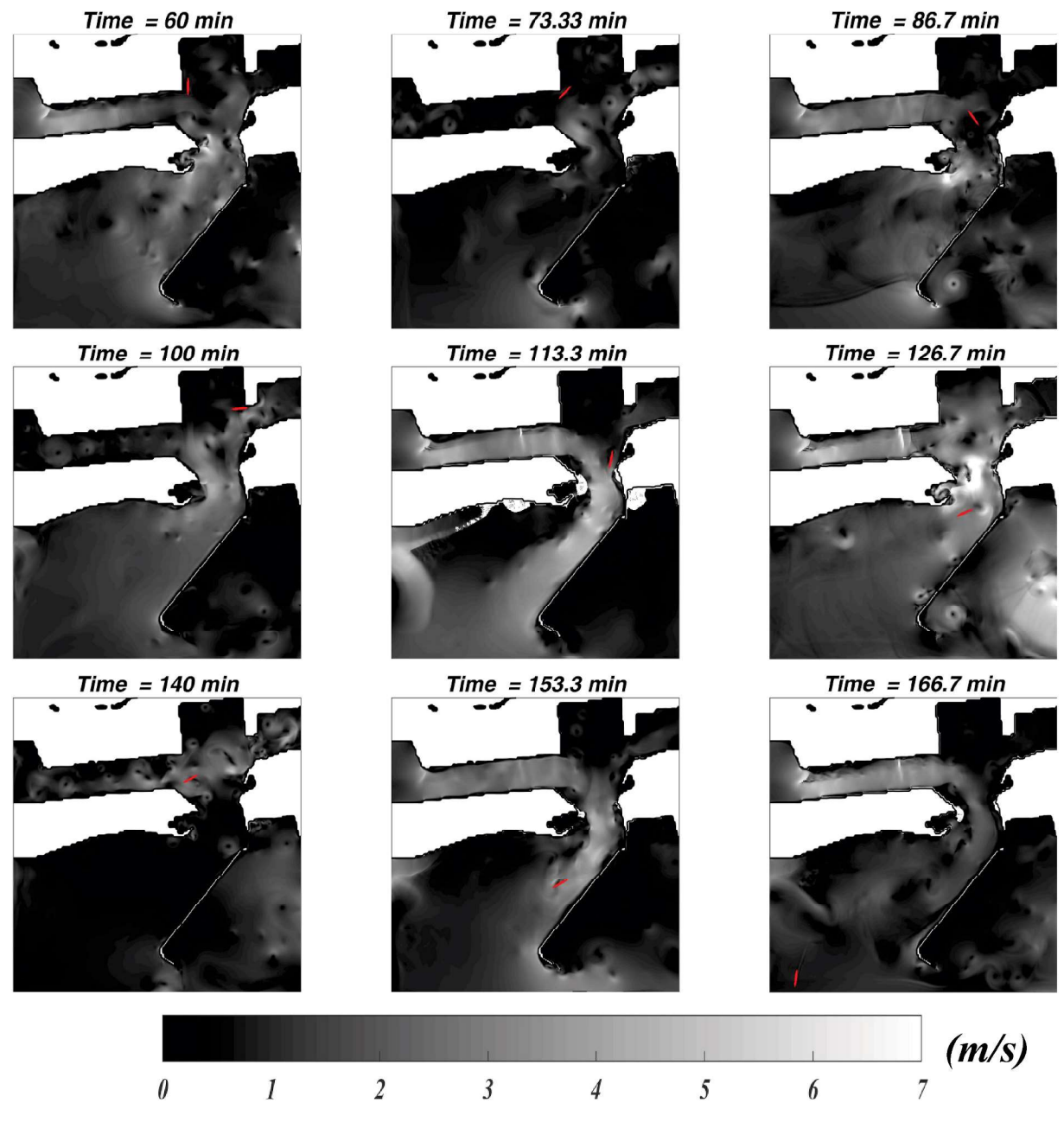
Length	Meters	177
Beam	Meters	26
Draft	Meters	6.1-9.0
Deadweight	Tons	32,500
Displacement	Cubic meters	20,000

were local, and relatively weak. Whilst the larger eddy generated at the center of the terminal in the baseline simulation also appeared in the one-ship case with a slight shift in south, the variations outside the terminal are negligible. On the other hand, in the multi-ship case the disparities in the predicted flow fields became more profound. Both in and out of the terminal, the flow patterns were altered drastically. As it has been put forward earlier, the presence of the vessels has a considerable impact on the flow fields not only near the vicinity of vessels but also at a broader area in and out of the terminal as can be seen from the plots given in the left panel of Fig. 12, which intensifies with the number of ships included in the analysis.

4.2. Incident of C.S. Victory in Ishinomaki Harbor during (2011) Tohoku Tsunami

Like the rest of the Tohoku coast, the Ishinomaki region in Miyagi prefecture was hit hard by the 2011 Tohoku Tsunami. In Ishinomaki city only, ~4000 casualties were reported, ~20,000 houses were completely destroyed, and entire port facilities were flooded (Takagi and Bricker, 2014). The C.S Viceroy, a 177-m-long bulk carrier was moored inside the Ishinomaki Harbor at the time of the tsunami. A personal communication with Dr. Tatsuya Asai revealed that approximately 66 min after the earthquake, around 16:00 JST, the ship broke all its moorings and started to drift freely inside the terminal until it was carried out of the port by the tsunami.

A realization of this incident is depicted here, using the dimensions and the physical properties of the vessel that are listed in Table 2. Since the precise draft of the ship at the time of the incident is unknown, in this analysis it was taken as $7.5~\mathrm{m}$; the midpoint of the minimum and maximum possible draft. The tsunami waves were brought to Ishinomaki Port through a nested grid system, where the final grid has the horizontal resolution of $5~\mathrm{m}$. The duration of the simulations in this innermost grid was $5~\mathrm{h}$. Initially, the C.S Viceroy was placed to the



 $\textbf{Fig. 13.} \ \ \textbf{Snapshots of the current field and the vessel's location at different instants.}$

mooring spot in the terminal where it was thought to be moored when the tsunami had arrived. Since the mooring lines were not included in this study, the vessel's motion had been restricted in the model for the first 66 min of the simulation, then it was released and let drift freely with the tsunami currents until the end of the run.

Snapshots of the simulation showing the motion of the vessel as well as the tsunami current fields, taken at the different times of the simulation after the ship was released are illustrated in Fig. 13 The figure shows that the speed of the tsunami currents entering to the terminal where the ship was residing about $\sim 3\ m/s$ around $t=60\ \rm mins$. This was approximately the time when the ship broke its mooring lines. A large eddy formed near the ship shortly after which pulled it away from the berth and carried it south near the terminal entrance. At around $t=90\ \rm mins$, the next tsunami surge has arrived and pushed the ship back in. After drifting and spinning with the flow in the port until $t\approx 150\ \rm mins$, finally it was taken out of the harbor and brought to the southern boundary of the computational domain.

However, as briefly discussed earlier, these parameters were in fact unknown a priori. Also, during the preliminary analysis, it has been noticed that if these parameters are changed in the beginning of the simulation, then the ship can follow a different path. Therefore, based on this observation, a sensitivity analysis was performed to better understand the role of the initial choice of these "free" parameters in model outputs.

The release time, draft and the initial location of the vessel in addition to the drag coefficient for the lateral current loading (C_{yc}) were selected for the sensitivity analysis. While, in general, the release time depends on the resultant forces on the hull along with the capacity of the vessel's mooring lines, the draft is determined by the total load (cargo + fuel). Similarly, the exact location of the vessel is an unknown, and moving the center of mass even by 1–2 grid points corresponds to 5–10 m of physical distance in the model, which can also lead to significant changes in exerted current forces. The drag coefficient (C_{yc}) is calculated empirically by Eqn. (38), which was derived by curve fitting to

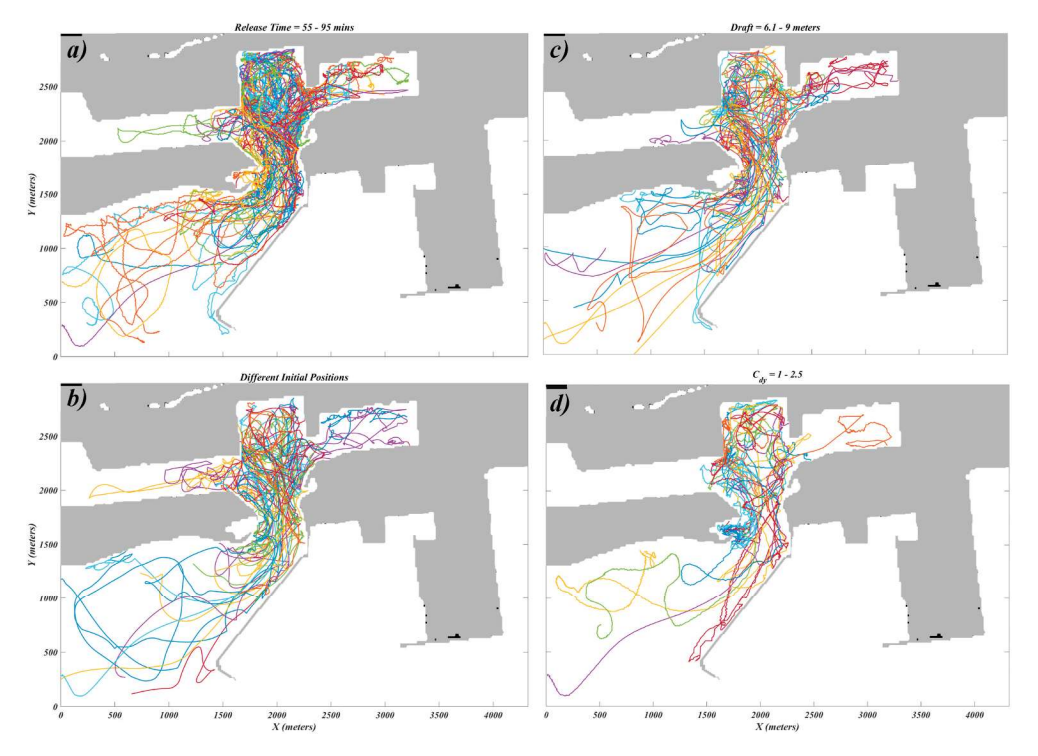


Fig. 14. The paths of the vessel estimated by the model for different values of a) Release time; b) Vessel draft; c) Initial location; d) Drag coefficient for lateral loading.

experimental date and aimed to be used by engineers. The coefficient can vary depending on the hull shape and the flow conditions, and therefore was included into this sensitivity analysis. The release time varied between 55 min and 95 min with 1-min increments, while the draft was increased by 0.1 m at each trial from 6.1 to 9 m. The initial center of mass moved 20 m laterally and longitudinally, which adds up to 16 trials, and the drag coefficient ranged from 1 to 2.5.

The results of the sensitivity analysis are summarized in Fig. 14, where all the paths calculated by the model for different initial values of different parameters after 5 h long simulations are shown. The figure tells that the model's outputs are very sensitive to the initial choice of parameters and even small changes in the release time, draft, initial location and the drag coefficient lead to remarkably different trajectories. These results indicate that the process is indeed random as no apparent trends or patterns can be identified from the figure. Although the model is capable of predicting the path of vessels for a given set of input parameter, unfortunately the randomness associated with the selection of the initial conditions implies that a single-simulation, deterministic approach for large vessel motion should be used qualitatively.

Nonetheless, the new insights offered by this study can aid the efforts to design ports that are resilient to tsunamis and provide guidance particularly to stakeholders in coastal communities during their disaster mitigation planning. As the hypothetical case from POLB suggests the presence of ships can change the flow conditions significantly within a port and they should be included in the simulations during tsunami hazard studies. Especially, deep draft vessels interfere with the flow, and neglecting them in analyses can lead to underestimation of tsunami hazard in mooring locations. Hence, a first order hazard assessment by utilizing the model presented here safe mooring spots within a port can be identified more accurately to plan to reduce the exposure to hazardous conditions as well as maintaining/upgrading the structures/infrastructure to help so, which overall can expand the harbor's ability to resist damage.

5. Conclusions

In this paper a collision and transport model were developed to predict the motion of large vessels within a port under the influence of strong currents generated by a tsunami. The transport module and the hydrodynamic solver are fully coupled, which allows flow and vessels to interact with each other. This aspect was ignored in earlier attempts and indeed is the key feature of this study. Considering the ratio of the draft of the large vessels (\sim 8–10 m) to the typical depths in ports (\sim 10–15 m), the interaction between the flow and the vessels is important. Therefore, for accurate representation of the flow field in the presence of the vessels consideration of their interaction is crucial.

The vessels were included into the hydrodynamic computations as free surface pressure distributions which also accounted for the form drag that the flow experiences due to vessels. Additionally, the bottom stress term was modified locally at the grid points where the pressure gradient was non-zero to include effect of the skin friction. Then, the capability of the modified hydrodynamic model was assessed first using the data provided in ER86 where the waves generated by the moving pressure disturbances had been investigated. It has been found that the model can sufficiently capture the amplitude and the phase of the leading wave for the pressure disturbances moving at the critical speed. Furthermore, the model was tested for the case when the flow passes a floating object, and the results were compared to a numerical benchmark test created in OpenFOAM. With the modifications made, MOST captured the generation, separation and the advection of the eddies generated in the lee of the floating block deftly when compared to the results obtained in OpenFOAM.

The transport model was based on the linear equations of motion and only three degrees of freedom are considered; surge, sway and the yaw. Added mass and the first order damping terms were included as the restoring hull forces, but the forces imposed by the ship's controls, thrusters and rudders were not. The reasoning behind this is the reports from past incidents emphasizing that once the vessel is picked-up by the flow, the ship's controls are of limited assistance in taking back the ship under control. Thus, the forces due to currents were the only sources of

the external loading. Moreover, the present model was also equipped with a built-in collision solver founded on the concept of the conservation of momentum and impulse. It can detect and evaluate the collisions between two or more vessels as well as the collisions that take place between the vessels and the port structures.

In the first test, the effects of a hypothetical tsunami arising from Alaska-Aleutians Subduction Zone was investigated for ships moored in the Port of Long Beach. Two different setups have been investigated here; one with a single ship moored within the port, and another with eight ships placed in and around the port. Then, the results from these two simulations were compared with the baseline simulation where no vessels were included. This analysis revealed that the flow in and around the vessels is indeed affected by the vessels and this gets intensified as the number of the vessels increases, and this should be considered in analysis for disaster mitigation planning.

The last large-scale test was based on an incident reported in Ishinomaki Port, Japan that happened during the 2011 Tohoku Tsunami. In this incident a \sim 180-m-long bulk carrier broke its mooring approximately 65 min after the first arrival of the tsunami and was taken out of the port after spinning and drifting freely inside the port. First, a realization of this event was simulated using the developed transport model, and then, a sensitivity analysis has been performed to see the effects of the parameters that cannot be known precisely before the incident. The results from these analyses showed that the model is capable of estimating the ship's path for certain combinations of input parameters, but at the same time the model results are very sensitive to the initial choice of the input parameters.

CRediT authorship contribution statement

Aykut Ayca: Conceptualization, Methodology, Software, Formal analysis, Investigation, Writing – original draft, Writing – review & editing, Visualization. **Patrick J. Lynett:** Conceptualization, Methodology, Resources, Writing – original draft, Supervision, Project administration, Funding acquisition.

Declaration of competing interest

The authors declare that they have no known competing financial interests or personal relationships that could have appeared to influence the work reported in this paper.

Acknowledgements

This material is based upon work supported in part by the California Geological Survey and National Science Foundation under Grants CMMI-1661052. Any opinions, findings, and conclusions or recommendations expressed in this material are those of the author(s) and do not necessarily reflect the views of the National Science Foundation. Additionally, we are grateful to Dr. Gökhan Güler for his help with setting up the OpenFOAM simulations. We would also like to thank Dr. Philippe Gondret for kindly sharing the experiment data of the bouncing spheres. Lastly, we thank two anonymous reviewers for their constructive comments.

References

- Adrian, R.J., Christensen, K.T., Liu, Z.-C., 2000. Analysis and interpretation of instantaneous turbulent velocity fields. Exp. Fluid 29 (3), 275–290. https://doi.org/ 10.1007/s003489900087.
- Akylas, T.R., 1984. On the excitation of long nonlinear water waves by a moving pressure distribution. J. Fluid Mech. 141, 455–466. https://doi.org/10.1017/ S0022112084000926.
- Bandyk, P.J., Beck, R.F., 2009. January). Nonlinear ship motion computations using a time-domain body-exact slender-body approach. In: ASME 2009 28th International Conference on Ocean, Offshore and Arctic Engineering. American Society of Mechanical Engineers, pp. 365–374. https://doi:10.1115/OMAE2009-79178.

Baraff, D., 1989. Analytical methods for dynamic simulation of non-penetrating rigid bodies, 3 In ACM SIGGRAPH Computer Graphics 23, 223–232.

- Barberopoulou, A., Borrero, J.C., Uslu, B., Legg, M.R., Synolakis, C.E., 2011. A second generation of tsunami inundation maps for the State of California. Pure Appl. Geophys. 168 (11), 2133–2146. https://doi.org/10.1007/s00024-011-0293-3.
- Bayraktar-Ersan, D., Beji, S., 2013. Numerical simulation of waves generated by a moving pressure field. Ocean Eng. 59, 231–239. https://doi.org/10.1016/j.ocean.eng. 2012.12.025.
- Bellotti, T., Theillard, M., 2019. A coupled level-set and reference map method for interface representation with applications to two-phase flows simulation. J. Comput. Phys. 392, 266–290. https://doi.org/10.1016/j.jcp.2019.05.003.
- Borrero, J.C., Lynett, P.J., Kalligeris, N., 2015a. Tsunami currents in ports. Phil. Trans. Math. Phys. Eng. Sci. 373 (2053), 20140372 https://doi.org/10.1098/rsta 2014 0372
- Blanke, M., Jansen, A., 1997. Dynamic properties of a container vessel with low metacentric height. Trans. Inst. Meas. Contr. 19 (2), 78–93. https://doi.org/ 10.1177/014233129701900203.
- Borrero, J.C., Bell, R., Csato, C., DeLange, W., Goring, D., Dougal Greer, S., Power, W., 2013. Observations, effects and real time assessment of the march 11, 2011 tohokuoki tsunami in New Zealand. Pure Appl. Geophys. 170 (6–8), 1229–1248. https:// doi.org/10.1007/s00024-012-0492-6.
- Borrero, J.C., Goring, D.G., Greer, S.D., Power, W.L., 2015b. Far-field tsunami hazard in New Zealand ports. Pure Appl. Geophys. 172 (3–4), 731–756. https://doi.org/ 10.1007/s00024-014-0987-4.
- Burwell, D., Tolkova, E., Chawla, A., 2007. Diffusion and dispersion characterization of a numerical tsunami model. Ocean Model. 19 (1–2), 10–30. https://doi.org/10.1016/ j.ocemod.2007.05.003.
- Cheung, K.F., Bai, Y., Yamazaki, Y., 2013. Surges around the Hawaiian Islands from the 2011 Tohoku tsunami. J. Geophys. Res. Oceans 118, 5703–5719. https://doi.org/ 10.1002/jgrc.20413.
- David, C.G., Roeber, V., Goseberg, N., Schlurmann, T., 2017. Generation and propagation of ship-borne waves-Solutions from a Boussinesq-type model. Coast Eng. 127, 170–187. https://doi.org/10.1016/j.coastaleng.2017.07.001.
- Dean, R.G., Dalrymple, R.A., 1991. Water wave mechanics for engineers and scientists. In: Advanced Series on Ocean Engineering, Pp. 295–325, World Scientific, Singapore.
- Dengler, L., Uslu, B., Barberopoulou, a., Borrero, J., Synolakis, C., 2008. The vulnerability of crescent city, California, to tsunamis generated by earthquakes in the kuril Islands region of the northwestern pacific. Seismol Res. Lett. 79 (5), 608–619. https://doi.org/10.1785/gssrl.79.5.608.
- Ertekin, R.C., Webster, W.C., Wehausen, J.V., 1986. Waves caused by a moving disturbance in a shallow channel of finite width. J. Fluid Mech. 169, 275–292. https://doi.org/10.1017/S0022112086000630.
- Fossen, T.I., 1994. Guidance and Control of Ocean Vehicles. John Wiles & Sons Inc., New York.
- Fritz, H.M., Phillips, D.A., Okayasu, A., Shimozono, T., Liu, H., Mohammed, F., Takahashi, T., 2012. The 2011 Japan tsunami current velocity measurements from survivor videos at Kesennuma Bay using LiDAR. Geophys. Res. Lett. 39 (2), 1–6. https://doi.org/10.1029/2011GL050686.
- Gondret, P., Lance, M., Petit, L., 2002. Bouncing motion of spherical particles in fluids. Phys. Fluids 14, 643–652. https://doi.org/10.1063/1.1427920.
- Gottschalk, S., Lin, M.C., Manocha, D., 1996, August. OBBTree: a hierarchical structure for rapid interference detection. In: Proceedings of the 23rd Annual Conference on Computer Graphics and Interactive Techniques, pp. 171–180.
- Green, A.C.M., E, A., Naghdi, P.M., 1976. A derivation of equations for wave propagation in water of variable depth. J. Fluid Mech. 78, 237–246.
- Hahn, J.K., 1988. Realistic animation of rigid bodies. In Acm Siggraph Computer Graphics 22 (1), 299–308 (ACM).
- Higuera, P., Lara, J.L., Losada, I.J., 2014. Three-dimensional interaction of waves and porous coastal structures using OpenFOAM®. Part I: formulation and validation. Coast Eng. 83, 243–258. https://doi.org/10.1016/j.coastaleng.2013.08.010.
- Johnson, J.M., Tanioka, Y., Ruff, L.J., Satake, K., Kanamori, H., Sykes, L.R., 1994. The 1957 great Aleutian earthquake. In: Shallow Subduction Zones: Seismicity, Mechanics and Seismic Potential. Birkhäuser, Basel, pp. 3–28. https://doi.org/ 10.1007/978-3-0348-7333-8 2.
- Johnson, J.M., Satake, K., 1997. Estimation of seismic moment and slip distribution of the April 1, 1946, Aleutian tsunami earthquake. J. Geophys. Res.: Solid Earth 102 (B6), 11765–11774. https://doi.org/10.1029/97JB00274.
- Kalligeris, N., Montoya, L., Ayca, A., Lynett, P., 2017. An approach for estimating the largest probable tsunami from far-field subduction zone earthquakes. Nat. Hazards 89 (1), 233–253. https://doi.org/10.1007/s11069-017-2961-9.
- Kamrin, K., Rycroft, C.H., Nave, J.-C., 2012. Reference map technique for finite-strain elasticity and fluid-solid interaction. J. Mech. Phys. Solid. 60 (11), 1952–1969. https://doi.org/10.1016/j.jmps.2012.06.003.
- Kanamori, H., 1970. The Alaska earthquake of 1964: radiation of long-period surface waves and source mechanism. J. Geophys. Res. 75 (26), 5029–5040. https://doi.org/ 10.1029/JB075i026p05029.
- Keen, A.S., Lynett, P.J., Eskijian, M.L., Ayca, A., Wilson, R., 2017. Monte Carlo-based approach to estimating fragility curves of floating docks for small craft marinas. J. Waterw. Port, Coast. Ocean Eng. 143 (4), 4017004 https://doi.org/10.1061/(ASCE)WW.1943-5460.0000385.
- Kim, D.H., Lynett, P.J., Socolofsky, S.A., 2009. A depth-integrated model for weakly dispersive, turbulent, and rotational fluid flows. Ocean Model. 27 (3–4), 198–214. https://doi.org/10.1016/j.ocemod.2009.01.005.
- Kobayashi, E.I., Yurugi, K., Koshimura, S., 2013. June). Evaluations of a ship evacuation maneuver from tsunami attack. In: ASME 2013 32nd International Conference on

- Ocean, Offshore and Arctic Engineering (Pp. V005T06A047-V005T06A047). American Society of Mechanical Engineers. https://doi.org/10.1115/OMAE2013-10624.
- Krueger, P., 2005. An over-pressure correction to the slug model for vortex ring circulation. J. Fluid Mech. 545, 427–443. https://doi.org/10.1017/ S0022112005006853.
- Lee, S.-J., Yates, G.T., Wu, T.Y., 1989. Experiments and analyses of upstream-advancing solitary waves generated by moving disturbances. J. Fluid Mech. 199, 569–593. https://doi.org/10.1017/S0022112089000492.
- Liu, P.L.-F., Wu, T.-R., 2004. Waves generated by moving pressure disturbances in rectangular and trapezoidal channels. J. Hydraul. Res. 42 (2), 163–171. https://doi. org/10.1080/00221686.2004.9628301.
- Lynett, P.J., Borrero, J.C., Weiss, R., Son, S., Greer, D., Renteria, W., 2012. Observations and modeling of tsunami-induced currents in ports and harbors. Earth Planet Sci. Lett. 327–328. 68–74. https://doi.org/10.1016/j.epsl.2012.02.002.
- Lynett, P.J., Borrero, J., Son, S., Wilson, R., Miller, K., 2014. Assessment of the tsunami-induced current hazard. Geophys. Res. Lett. 41 (6), 2048–2055. https://doi.org/10.1002/2013GL058680.
- Ma, G., Shi, F., Kirby, J.T., 2012. Shock-capturing non-hydrostatic model for fully dispersive surface wave processes. Ocean Model. 43, 22–35. https://doi.org/ 10.1016/j.ocemod.2011.12.002.
- Ma, G., Farahani, A.A., Kirby, J.T., Shi, F., 2016. Modeling wave-structure interactions by an immersed boundary method in a σ-coordinate model. Ocean. Eng. 125, 238–247. https://doi.org/10.1016/j.oceaneng.2016.08.027.
- Menter, F.R., 1994. Two-equation eddy-viscosity turbulence models for engineering applications. AIAA J. 32 (8), 1598–1605. https://doi.org/10.2514/3.12149.
- Mimeau, C., Mortazavi, I., 2021. A review of vortex methods and their applications: from creation to recent advances. Fluid 6, 68. https://doi.org/10.3390/fluids6020068.
- Moore, M., Wilhelms, J., 1988. Collision detection and response for computer animation. In ACM Siggraph Computer Graphics 22 (1), 289–298.
- Morgan, M.J., 1978. Dynamic Positioning of Offshore Vessels.
- Okal, E.A., Fritz, H.M., Raad, P.E., Synolakis, C., Al-Shijbi, Y., Al-Saifi, M., 2006a. Oman field survey after the December 2004 Indian Ocean tsunami. Earthq. Spectra 22 (3). https://doi.org/10.1193/1.2202647.
- Okal, E.A., Fritz, H.M., Raveloson, R., Joelson, G., Pančošková, P., Rambolamanana, G., 2006b. Madagascar field survey after the December 2004 Indian Ocean tsunami. Earthq. Spectra 22 (3). https://doi.org/10.1193/1.2202646.
- Okal, E.A., Sladen, A., Okal, E.A.S., 2006c. Rodrigues, Mauritius, and R??union Islands field survey after the December 2004 Indian Ocean tsunami. Earthq. Spectra 22 (3). https://doi.org/10.1193/1.2209190.
- Perez, T., Blanke, M., 2002. Mathematical Ship Modeling for Control. Technical University of Denmark, pp. 1–22. http://www.iau.dtu.dk/secretary/pdf/TP-MB-ship mod pdf
- Peskin, C.S., 2002. The immersed boundary method. Acta Numer. 11, 479–517. https://doi.org/10.1017/S0962492902000077.
- Price, W.G., Bishop, R.E.D., 1974. Probabilistic Theory of Ship Dynamics. Halsted Press. Rakhsha, M., Pazouki, A., Serban, R., Negrut, D., 2019. Using a half-implicit integration
- scheme for the SPH-based solution of fluid-solid interaction problems. Comput. Methods Appl. Mech. Eng. 345, 100–122. https://doi.org/10.1016/j.cma.2018.09.027.
- Ruiz-Villanueva, V., Bladé, E., Sánchez-Juny, M., Marti-Cardona, B., Díez-Herrero, A., Bodoque, J.M., 2014a. Two-dimensional numerical modeling of wood transport. J. Hydroinf. 16 (5), 1077–1096. https://doi.org/10.2166/hydro.2014.026.

- Ruiz Villanueva, V., Bladé Castellet, E., Díez-Herrero, A., Bodoque, J.M., Sánchez-Juny, M., 2014b. Two-dimensional modelling of large wood transport during flash floods. Earth Surf. Process. Landforms 39 (4), 438–449. https://doi.org/10.1002/esp.3456
- Sakakibara, S., Takeda, S., Iwamoto, Y., Kubo, M., 2010. A hybrid potential theory for predicting the motions of a moored ship induced by large-scaled tsunami. Ocean. Eng. 37 (17–18), 1564–1575. https://doi.org/10.1016/j.oceaneng.2010.09.005.
- Satake, K., 1995. Linear and nonlinear computations of the 1992 Nicaragua earthquake tsunami. Pure Appl. Geophys. 144 (3-4), 455-470. https://doi.org/10.1007/ BF00874378.
- Shi, F., Kirby, J.T., Harris, J.C., Geiman, J.D., Grilli, S.T., 2012. A high-order adaptive time-stepping TVD solver for Boussinesq modeling of breaking waves and coastal inundation. Ocean Model. 43, 36–51. https://doi.org/10.1016/j. ocemod.2011.12.004.
- Skejic, R., Faltinsen, O.M., 2008. A unified seakeeping and maneuvering analysis of ships in regular waves. J. Mar. Sci. Technol. 13 (4), 371–394. https://doi.org/10.1007/ s00773-008-0025-2.
- Sorensen, R.M., 1973. Ship-generated waves. Adv. Hydrosci. 9, 49-83.
- Sun, P., Le Touzé, D., Oger, D., Zhang, A.(, 2021. An accurate FSI-SPH modeling of challenging fluid-structure interaction problems in two and three dimensions. Ocean. Eng. 221, 108552 https://doi.org/10.1016/j.oceaneng.2020.108552.
- Takagi, H., Bricker, J.D., 2014. Assessment of the effectiveness of general breakwaters in reducing tsunami inundation in Ishinomaki. Coast Eng. J. 56 (4), 1450011–1450018. https://doi.org/10.1142/S0578563414500181.
- Terzopoulos, D., Platt, J., Barr, A., Fleischer, K., 1987. Elastically deformable models. ACM Siggraph Computer Graphics 21 (4), 205–214.
- Titov, V., Synolakis, C., 1998. Numerical modeling of tidal wave runup. J. Waterw. Port, Coast. Ocean Eng. 124 (4), 151–171. https://doi.org/10.1061/(ASCE)0733-950X (1992)1444(157)
- Titov, V., Kânoğlu, U., Synolakis, C., 2016. Development of MOST for real-time tsunami forecasting. J. Waterw. Port, Coast. Ocean Eng. 142 (6), 03116004 https://doi.org/10.1061/(ASCE)WW.1943-5460.0000357.
- Tomita, T., Honda, K., 2011. Practical model to estimate drift motion of vessels by tsunami. Coast. Eng. Proc. 1(32) https://doi.org/10.9753/icce.v32.management.27.
 U.S. Army Corps of Engineers, 2005. Design: Moorings, Unified Facilities Criteria. UFC 4-159-3. Washington. DC.
- Wilson, R.I., Admire, A.R., Borrero, J.C., Dengler, L.A., Legg, M.R., Lynett, P., Whitmore, P.M., 2013. Observations and impacts from the 2010 Chilean and 2011 Japanese tsunamis in California (USA). Pure Appl. Geophys. 170 (6–8), 1127–1147. https://doi.org/10.1007/s00024-012-0527-z.
- Wilson, R., Davenport, C., Jaffe, B., 2012. Sediment scour and deposition within harbors in California (USA), caused by the March 11, 2011 Tohoku-oki tsunami. Sediment. Geol. 282, 228–240. https://doi.org/10.1016/j.sedgeo.2012.06.001.
- Wu, K., Yang, D., Wright, N., 2016. A coupled SPH-DEM model for fluid-structure interaction problems with free-surface flow and structural failure. Comput. Struct. 177, 141–161. https://doi.org/10.1016/j.compstruc.2016.08.012.
- Xiong, Y., Mahaffey, S., Liang, Q., Rouainia, M., Wang, G., 2020. A new 1D coupled hydrodynamic discrete element model for floating debris in violent shallow flows. J. Hydraul. Res. 58 (5), 778–789. https://doi.org/10.1080/ 00221686.2019.1671513.
- Zhan, L., Peng, C., Zhang, B., Wu, W., 2019. A stabilized TL–WC SPH approach with GPU acceleration for three-dimensional fluid–structure interaction. J. Fluid Struct. 86, 329–353. https://doi.org/10.1016/j.jfluidstructs.2019.02.002.